Surface freezing in chain molecules: Normal alkanes

B. M. Ocko,[1] X. Z. Wu,[2,3] E. B. Sirota,[4] S. K. Sinha,[5] O. Gang,[6] and M. Deutsch[6]
[1]*Physics Department, Brookhaven National Laboratory, Upton, New York 11973*
[2]*Physics Department, Northern Illinois University, DeKalb, Illinois 60115*
[3]*Material Sciences Division, Argonne National Laboratory, Argonne, Illinois 60439*
[4]*Exxon Research and Engineering Company, Route 22 East, Annandale, New Jersey 08801*
[5]*Advanced Photon Source, Argonne National Laboratory, Argonne, Illinois 60439*
[6]*Physics Department, Bar Ilan University, Ramat Gan 52900, Israel*
(Received 9 October 1996)

A rare surface freezing phenomenon is observed in molten normal alkanes, using x-ray and surface tension measurements. An ordered monolayer forms on the surface of the liquid alkane at temperatures up to 3 °C above the bulk freezing temperature T_f. The structure of the monolayer was studied in detail for a wide range of molecular lengths and temperatures. The single layer formed persists down to T_f. The rare surface phase exists only for carbon numbers of $16 \leqslant n \leqslant 50$. The molecules in the layer are hexagonally packed and show three distinct ordered phases: two rotator phases, with molecules oriented vertically ($16 \leqslant n \leqslant 30$) and tilted towards nearest neighbors ($30 < n < 44$) and one crystalline phase with molecules tilted towards next-nearest neighbors ($n \geqslant 44$). The temperature dependence of the surface tension and the range of existence vs carbon number are satisfactorily accounted for within a simple theory based on surface energy considerations. [S1063-651X(97)12003-7]

PACS number(s): 68.10.−m, 61.25.Em, 64.70.Dv

I. INTRODUCTION

Normal alkanes are linear hydrocarbon chains, some of the simplest organic molecules. They are also the main building blocks of lipids, surfactants, liquid crystals, polymers, and many other, more complex organic compounds. The basic properties of these complex molecules will be influenced, and in many case even dominated, by those of the alkanes. In addition to their fundamental scientific interest, alkanes are also of great interest to applied science and industry, as basic constituents of crude petroleum and of many pharmaceutical and petroderivative products. It is not surprising, therefore, that the bulk properties of alkanes were, and are still being investigated vigorously and extensively [1–5]. What *is* surprising, is the fact that their surface structure and properties have received very little attention, in spite of the decisive role of the interface in important applications such as catalysis, chemical reactions, product bonding, drug release and delivery, and many more.

We have recently undertaken an extensive study of the surface structure of chain molecule melts [6–8] and their mixtures [9] near their bulk freezing temperatures. The dependence of the structure on the temperature, chain length, and end groups was studied in detail. We present here the first part of this study, which deals with the surface structure of pure, single-component melts of normal alkanes. The most surprising discovery is that these molecules show surface freezing, whereby a single crystalline monolayer is formed at the surface of the isotropic liquid bulk at temperatures up to ~3 °C above the bulk freezing temperature T_f, for a range of carbon numbers n. Light scattering [10] and ellipsometric [11] studies confirm our findings of surface freezing in alkanes. This very rare surface ordering phenomenon was hitherto observed only in liquid crystals [12–14], and even there the surface layers have almost always only smectic *A* (liquidlike in-plane) order, rather than a full crystalline one, as is the case here. In this section we discuss this effect in general, after discussing the basic structure of the molecule and some related solid bulk properties. We also address the similarities and assimilarities between the surface crystalline layer and water-supported Langmuir films. Sections II–IV deal with the experimental details, the presentation and discussion of our results, and the conclusions emerging from this study.

A. Basic structure

Normal alkanes have the general formula CH_3—$(CH_2)_{n-2}$—CH_3 (abbreviated as C_n). As shown in Fig. 1, the carbon-carbon (C—C) bond length is 1.54 Å and the angle between two C—C bonds is [1] 112°. Any three neighboring carbons (two neighboring bonds) define, therefore, a plane, relative to which a fourth carbon can assume one of three orientational positions, shown in Fig. 1(b). The global energy minimum position is for the fourth carbon to remain in the plane defined by the other three carbons (a *trans* bond). Two local energy minima are obtained for the fourth carbon rotated 120° off that plane (*gauche* bonds). The energy difference between the *trans* and *gauche* bonds depends on the intra- and interchain interactions. In the bulk crystalline phases at low temperatures, the energy difference between the *trans* and *gauche* bond is significantly more than k_bT, therefore almost all bonds remain in the lowest, *trans*, conformation and all carbons of a single n-alkane molecule reside on the same plane. The molecule is then straight, with a length of $(n-1)1.27$ Å between the terminal carbon atoms, where 1.27 Å $=1.54$ Å $\sin(112°/2)$ is the projection of the bond length on the chain axis. In the liquid phase, at high temperatures, the energy difference between *trans* and *gauche* bonds becomes smaller than k_bT. The chain then

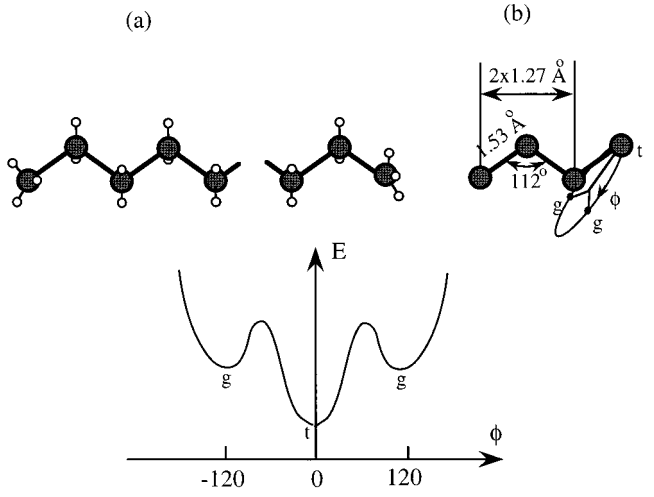

FIG. 1. (a) The structure of the *n*-alkane molecule. (b) The bond conformations and structural parameters, showing the positions for *trans* (t) and *gauche* (g) conformations. The corresponding energy has two local minima for the g positions and a global one for the t.

becomes flexible and bonds may be excited into *gauche* conformations, rendering the molecule nonlinear and aplanar.

In addition to the usual liquid and crystalline phase, the bulk alkanes exhibit a sequence of intermediate plastic crystalline phases known as rotator phases [1–5,15–17]. The rotator phases are crystals with three-dimensional (3D) long-range positional order of their centers of mass, but no long-range order in the rotational degree of freedom of a molecule about its long axis. Short-range order in these correlations does exist, and increases as temperature is reduced. Five rotator phases have been identified in the bulk alkanes distinguished by the lattice distortion (δ), tilt magnitude (θ), and direction (ϕ) [17]. The distortion is defined as the difference from unity of the ratio of the minor to major axis of an ellipse drawn through the six ''nearest'' neighbors when viewed along the axis of the chains. The rotator phases of interest in this study are those which occur at the highest temperature, immediately below T_f. The rotator phase with the highest symmetry is the R_{II} phase in which the molecules are pointing along the layer normal and are, on average, packed hexagonally. Thus, $\delta=0$ in this phase, which is the highest temperature bulk rotator phase for carbon numbers $22\leqslant n\leqslant 25$. At lower temperatures (reached via a first order transition) the R_I phase occurs. The in-plane R_I structure is distorted hexagonal (orthorhombic). For $n<22$, the alkanes melt directly from the R_I phase, without going through the R_{II} phase. However, the R_{II} phase is easily induced in binary mixtures of shorter chain lengths [2]. For $n\geqslant 26$, the highest temperature rotator phase is the R_{IV} phase where the molecules are tilted toward next-nearest neighbors by an angle θ. The distortion δ in this phase is finite, but small, and is considered a secondary effect, induced by coupling between θ and δ. The tilt magnitude in the R_{IV} phase increases with increasing chain length above $n=26$. The rotator phases can be distinguished from the crystal phases by the area per molecule (as viewed along the chain axis), which is ~ 19.5 Å^2 in the rotator phases and ~ 18.5 Å^2 in the crystal phases.

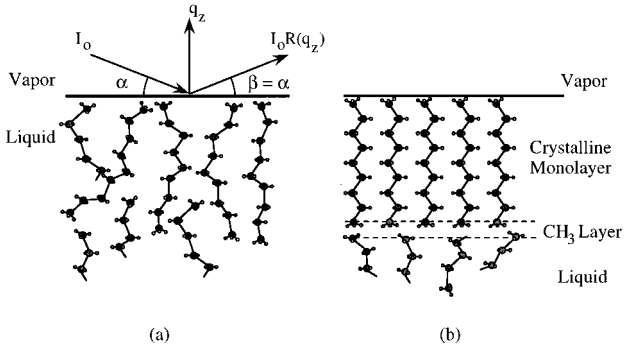

FIG. 2. (a) The x-rays reflected specularly from the vapor-liquid interface of *n*-alkanes at high enough temperatures, at which the molecules are flexible. (b) The surface crystalline layer of *n*-alkanes below surface freezing temperatures, but still above the bulk freezing point.

As we shall see below, alkane surface monolayers for $n\leqslant 30$ adopt a structure similar to that of the R_{II} bulk phase, while for $n>30$ they resemble the tilted bulk phases. The surface-frozen and liquid surface structures are shown in Fig. 2.

B. Surface freezing

It has long been realized that dimensionality has a profound influence on the phase behavior of matter, and, hence, the phase sequences of thin films and surfaces were expected [18], and found experimentally [19], to differ from those of the 3D bulk. Both theory and experiment show that with very few exceptions it is the *less ordered surface* phase which coexists with the *more ordered bulk* phase, i.e., the surface melts at a lower temperature than the bulk. This phenomenon, called surface melting, has been discovered in almost all solids studied [19]. This is easy to rationalize since the surface molecules are generally less constrained than those in the bulk and possess, therefore, a higher entropy. A much less common, and less understood phenomenon is surface freezing, where an *ordered surface* layer coexists with a *disordered bulk* liquid. This effect has been observed so far only in liquid crystals [12,14,20], where, however, smectic surface layers are observed to grow on the vapor-nematic or the vapor-isotropic liquid interfaces, and hexatic [21,22] and crystalline-*B* [23] phases were observed at the surfaces of free-standing smectic films. However, no true crystalline surface phase was ever observed over a disordered (nematic or isotropic) bulk. It has been speculated that these rare phenomena are related to the chainlike geometry of the molecules, or to their hydrocarbon tails. Thus, investigation of the surface phase behavior of the simplest linear hydrocarbons, namely, normal alkanes, may shed some light on similar phenomena in the much more complicated liquid crystal molecules. However, allowance must be made for the significant geometric and chemical differences between alkanes and liquid crystals. Alkanes are simple, uniform molecules, interacting almost exclusively via van der Waals interactions. They are flexible at higher temperatures and rigid at lower temperatures. By contrast, liquid crystal molecules are composed of a permanently rigid core to which hydrocarbon tails are attached and have rather complex interactions, reflected in their rich phase diagram even above their crystalline phases.

C. Langmuir films

Langmuir films are single monolayers of amphiphilic molecules (usually alkane chains with one CH_3 headgroup replaced by a polar moiety) spread on the free surface of water or any other nonsolvent subphase. The molecules have their hydrophilic headgroups in the water and their hydrophobic tails pointing away from it [24–26]. Structural studies revealed a rich quasi-2D phase diagram in these films, depending on the molecular shape, area per molecule, temperature, etc. [27,28]. It would, therefore, seem natural to consider an analogy between Langmuir films and our system. Such an analogy must be drawn, however, with caution. Although rarely discussed, the subphase of Langmuir films has an all-important role in the determination of the behavior of the system: it confines the molecules to a 2D ''universe,'' which they probably would not assume under their own intermolecular interactions. In fact, in the majority of cases this confinement is the strongest interaction in the system. This dominant influence is considerably reduced in our case, since the surface molecules may exchange freely with those of the bulk. Thus, for example, it is clear that the surface pressure cannot be varied in our case, as it is in Langmuir films: upon reducing the surface area our surface layer would relieve the pressure by ejecting molecules into the bulk, keeping the area per molecule fixed at the value favored by the molecular interactions of the uncompressed layer. The interplay between the surface and bulk free energies, and the subtle difference in the free energy of a molecule in the bulk and at the surface, control the formation and phase behavior of the crystalline monolayer in our system, rather than the 2D confinement imposed by the surface of the water. Thus, even though some of the structures may be similar in the two systems, the underlying interactions and thermodynamics may be considerably different.

II. EXPERIMENT

We have studied the structure at the vapor-liquid interface of normal alkanes by x-ray reflectivity and grazing incidence diffraction and the thermodynamics by surface tension measurements. We now discuss the various experimental issues in detail.

A. The sample cells

Both the x-ray and surface tension experiments were done with samples in temperature controlled cells. The cell for the x-ray experiments consists of a two stage oven, with a passive outer stage and a temperature controlled inner stage. The outer can is made of aluminum with aluminum coated Mylar windows. The inner cell consists of a solid beryllium cylinder (of 3 in. i.d.) with a uniform wall thickness of 0.5 mm, resulting in an x-ray attenuation factor of $\sim 30\%$. This all-beryllium construction provides a wide range of x-ray access. The beryllium cylinder can be Viton O-ring sealed with top and bottom copper plates, however, no differences could be observed between data taken with a loosely sealed and an air tight cell. The two copper plates are identical so that good thermal homogeneity can be achieved. Heaters are attached to the outer surfaces of these two plates and thermistors are imbedded in them. For those samples which require subroom temperature measurements, thermoelectric cooling elements are attached to the outer surfaces of the bottom copper plate. The short term (~ 1 h) temperature stability is $\leqslant 0.005\,^{\circ}\mathrm{C}$ and the long term (~ 1 day) $\sim 0.05\,^{\circ}\mathrm{C}$. The measured temperature homogeneity across the x-ray illuminated area on the sample is $\sim 0.005\,^{\circ}\mathrm{C}$. An 0.5 mm thick silicon wafer placed directly on the bottom copper plate was used as the sample substrate. A liquid sample a fraction of a mm high was deposited on the wafer and contained there by its own meniscus.

The cell used for the surface tension measurements is an aluminum cell surrounded by thermal insulation. The cell is heated from both top and bottom, and can also be cooled by thermoelectric elements attached to the bottom. This cell cannot be fully sealed, since the wire supporting the Wilhelmy plate has to pass through the top to connect to the balance. However, since the vapor pressures of alkanes near their freezing points are small, the small hole at the top plate does not influence the experimental results, as verified by the excellent agreement with the x-ray measurements.

B. The samples

1. Sample preparation

Samples are purchased from Sigma, Aldrich, and Fluka. They are labeled as $\geqslant 98\%$ pure, and are used as received. About one gram of liquid alkane is spread over a 3 in. diam silicon wafer. The sample thickness is about ~ 0.2 mm, which is thick enough to form a large flat surface area and absorb the x-rays which may penetrate it and be reflected from the liquid-silicon interface. Yet, it is thin enough to damp out any mechanical vibrations on the vapor-liquid interface and be contained on the silicon wafer by its own meniscus.

2. The role of the sample purity

The $\geqslant 98\%$ purity of the sample, though high, would still allow more than enough impurities to cover the surface if they are more surface active than the alkane studied. However, the surface crystalline structures deduced from the x-ray experiments show unambiguously that the molecules in the crystalline surface phase have to be at least very similar in size and shape, if not identical, to the n-alkane of the bulk. The possible surface impurities are limited, therefore, to n-alkanes or n-alkane derivatives of similar carbon numbers. In our systematic surface studies of binary n-alkane mixtures [9] we found that the composition in the surface crystalline layer is very similar to that in the bulk for mixtures where there is only a small difference in the lengths of the two components. This would yield in our case a $<2\%$ impurity content in the surface layer for different-length n-alkane impurities. A few other common types of impurities, of shape similar to that of alkanes, may also be excluded. For example, fatty acids show no formation of a surface layer at all [29], while alcohols show the formation of a bilayer on the surface, which, if formed, would be easily distinguishable from the monolayer observed. The study of these most common impurities, as well as the systematic variation of the measured structural and thermodynamic quantities with the molecular length and their correspondence with the bulk rotator phase structure and properties, provide irrefutable evi-

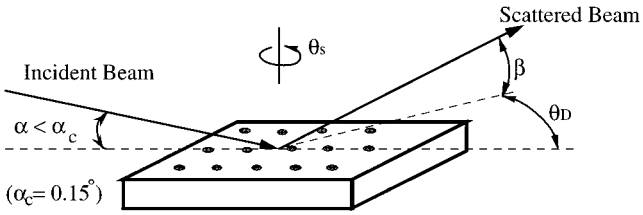

FIG. 3. The geometry for measurements of the in-plane structures of the surface layer.

dence that the surface crystalline layer indeed consists of the n alkane studied and its formation is an intrinsic property of the pure material.

Regardless of this conclusion, it seems that impurities may play a role in the *kinetics* of the surface crystallization, as do impurities in bulk crystallization [30]. In particular, we observe some discrepancy between the x-ray and surface tension measurements: while surface freezing was detected in surface tension measurements in all n-alkane samples of $16 \leqslant n \leqslant 50$, it did not show up in x-ray measurements in certain production lots of a few samples. The same effect was also observed and studied by Thomas [31] for a well purified C_{17} sample, where minute amounts of impurities had to be added to induce surface freezing, while the actual nature of the impurity seemed to be unimportant. This, and our experience, indicate that impurities may be essential in nucleating the surface crystals. The Wilhelmy plate in the surface tension measurements may provide ample nucleation sites for the surface crystal, while in x-ray studies these nucleation sites are not available and thus very slow layer formation kinetics may result. Further systematic studies are required to elucidate the role of impurities in the kinetics of the layer formation.

C. Spectrometer

The x-ray measurements were carried out on the Harvard-BNL Liquid Surface Diffractometer at National Synchrotron Light Source, beamline X22B, with a wavelength $\lambda \approx 1.54$ Å. The details of this spectrometer were described elsewhere [34]. Since the liquid surface is always horizontal, the x-rays emerging horizontally from the beamline have to be tilted down to impinge on the sample's surface at some angle of incidence α . This is achieved by Bragg reflecting the beam from a Ge(111) crystal. The angle α is varied by rotating this crystal about an axis coinciding with the horizontal beam by means of a vertical Euler circle at the center of which the crystal is mounted. The sample's vertical position is adjusted to intercept the beam at each α. The detection arm can be adjusted to vary the detection angle β with respect to the horizontal and the detection angle θ_D transverse to the reflection plane (see Fig. 3). In this configuration, both the surface-normal and surface-parallel components of the wave-vector transfer, q_z and q_r, are given in terms of α, β and θ_D by

$$q_z = (2\pi/\lambda)(\sin\alpha + \sin\beta), \tag{1}$$

$$q_r = (2\pi/\lambda)\sqrt{\cos^2\alpha + \cos^2\beta - 2\cos\alpha\cos\beta\cos\theta_D} \approx (4\pi/\lambda)\sin(\theta_D/2). \tag{2}$$

D. Reflectivity

The specular reflection is measured by placing the detector in the reflection plane ($\theta_D = 0$), and at a detection angle $\beta = \alpha$. In this geometry, the wave-vector transfer is normal to the surface, $q_z = (4\pi/\lambda)\sin\alpha$ and $q_r = 0$. Thus, the reflectivity $R(q_z)$, the intensity of specular reflection normalized by the incident one as a function of q_z, yields information on the electron density profile normal to the surface.

The horizontal size of the incident beam is always set to be less than 1 mm and the vertical size is changed with the incident angle from 0.05 mm at small angles (to ensure a beam footprint smaller than the sample size) to 0.4 mm at large angles (to achieve maximum intensity where the reflectivity is low). To limit the divergence of the beam after the beam-defining slits, a second pair of slits upstream of the toroidal focusing mirror were utilized at the smallest α. The slits in front of the detector, positioned 600 mm away from the sample, are open 2 mm vertically and 4 mm horizontally. The background is taken either by (1) offsetting β and α such that $\beta \neq \alpha$, but keeping $\alpha + \beta$ fixed, or (2) by moving the detector transverse to the reflection plane by setting $\theta_D \neq 0$. In either case, the offset must be sufficiently large to ensure picking up only the background and no part of the reflected signal. The background slopes with the offset using (1) but is roughly constant using (2). In either case the background under the reflection peak is easy to determine and subtract off.

For an ideally flat and sharp surface dividing a vapor half-space (of electron density $\rho_e = 0$) from a liquid half-space ($\rho_e = \text{const} > 0$), the reflectivity $R(q_z)$ is given by the Fresnel reflectivity $R_F(q_z)$

$$R_F(q_z) = \left| \frac{q_z - \sqrt{q_z^2 - q_c^2}}{q_z + \sqrt{q_z^2 - q_c^2}} \right|^2, \tag{3}$$

with $q_c = (4\pi/\lambda)\sin\alpha_c$ and the critical angle $\alpha_c \approx \sqrt{r_e \rho_e \lambda^2/\pi}$. r_e is the classical electron radius. Absorption is neglected here, as its only effect in our case is near the critical angle and is quite minor. $R_F(q_z)$ is unity for $q < q_c$, and decreases as $(q_c/2q_z)^4$ for $q_z \gg q_c$. For a surface layer having an electron density different from the bulk, the x-rays reflected from its upper and lower interfaces interfere in the far field to produce modulations in the reflectivity $R(q_z)$, akin to the well known Kiessig fringes in optics. The period of the modulation Δq_z is related to the layer thickness D as $\Delta q_z = 2\pi/D$, and the amplitude of the modulations depends on the electron density difference between the layer and the bulk.

An arbitrary density profile can always be sliced into many thin layers, within each of which the electron density can be assumed to be constant. At each interface between two layers, x-rays are both reflected and transmitted. The amplitude of the reflected wave, normalized by the incident one, is defined as the reflection coefficient r. The normalized amplitude of the transmitted wave, i.e., transmission coefficient t, is related to the reflection coefficient r as $t = 1 - r$. The reflection coefficient r is given by

$$r = \frac{\sqrt{q^2 - q_{c1}^2} - \sqrt{q^2 - q_{c2}^2}}{\sqrt{q^2 - q_{c1}^2} + \sqrt{q^2 - q_{c2}^2}}, \tag{4}$$

where q_{c1} and q_{c2} are the critical wave vectors of the two layers. Define waves moving into the interface by a vector

$$A\begin{pmatrix}1\\0\end{pmatrix},$$

and waves moving away from it by a vector

$$B\begin{pmatrix}0\\1\end{pmatrix}.$$

Then, the amplitudes of waves at the two sides of the interface are related by a matrix **S**

$$\begin{pmatrix}A_-\\B_-\end{pmatrix}=\mathbf{S}\begin{pmatrix}A_+\\B_+\end{pmatrix}\quad\text{with}\quad\mathbf{S}=\frac{1}{1+r}\begin{pmatrix}1&r\\r&1\end{pmatrix}. \tag{5}$$

In one uniform layer of thickness D, a wave is propagated from one interface $(z=0)$ to the other $(z=D)$ by the propagation matrix **P**

$$\begin{pmatrix}A_{z=0}\\B_{z=0}\end{pmatrix}=\mathbf{P}\begin{pmatrix}A_{z=D}\\B_{z=D}\end{pmatrix}\quad\text{with}\quad\mathbf{P}=\begin{pmatrix}\exp(ikD)&0\\0&\exp(-ikD)\end{pmatrix}. \tag{6}$$

Therefore the x-ray reflection and transmission of the whole density profile is characterized by one matrix **M**, which is the product of all the relevant interface and propagation matrices **S** and **P**. The reflectivity R can be derived from M as: $R=|M_{21}/M_{11}|^2$. The effect of interfacial roughness is included by multiplying the reflection coefficient r at each interface by a Debye-Waller-like factor $\exp(-q_z^2\sigma_i^2/2)$. The x-ray absorption in a layer can also be included in the propagation matrix, but its effect is negligible in our case. The shape of the actual density profile can be determined by adjusting the number of layers, their thicknesses D_i, densities ρ_i, and interfacial roughnesses σ_i, until a good agreement of the resultant calculated reflectivity with the measured one is obtained. Further details can be found in Refs. [32,33]. As detailed below, for the crystalline surface layer on a liquid alkane bulk, we used a density profile of two different slabs, each with a uniform density.

E. Surface roughness

Across the bulk-vapor interface of a liquid, the electron density drops monotonically and smoothly from the constant value of the bulk liquid to zero for the vapor phase. The intrinsic width of the interface, σ_0, is determined by the atomic form factor and is smaller than the molecular size. However, since there always exist thermally excited capillary waves on the surface, the interface width is broadened from σ_0 to a much larger value. For x-ray reflectivity experiments, the effective interfacial width σ_{eff} comes from both σ_0 and the contributions from those thermally excited capillary waves whose wavelengths are between the upper cutoff, $q_{\max}\approx\pi/a$, where a is of order of the molecular size, and the lower cutoff, $q_{\min}\approx q_z\Delta\beta/2$, determined by the instrumental resolution through $\Delta\beta$, which is the angular acceptance of the detector in the plane of reflection

$$\sigma_{\text{eff}}^2=\sigma_0^2+\frac{k_bT}{2\pi\gamma}\ln\left(\frac{2q_{\max}}{q_z\Delta\beta}\right). \tag{7}$$

Here k_b is the Boltzman constant, T—the temperature and γ—the surface tension. The measured reflectivity $R(q_z)$ deviates in this case from the Fresnel reflectivity $R_F(q_z)$ of an ideally flat surface by a Debye-Waller-like factor

$$R(q_z)=R_F(q_z)\exp(-q_z^2\sigma_{\text{eff}}^2). \tag{8}$$

The above expressions for the x-ray reflectivity from liquid surfaces have been verified with a number of simple liquids [34]. We have further examined these two expressions for liquid n-alkane surfaces of different chain lengths over a large temperature range above the surface freezing point [35]. In principle, σ_{eff} is q_z dependent. However, in practice, since the $\exp(-q_z^2\sigma_{\text{eff}}^2)$ factor in $R(q_z)$ becomes important only at large q_z, the reflectivity of a liquid surface can be very well approximated by replacing the q_z dependent σ_{eff} in the Eq. (7) with a constant σ_{eff}, the value of which is determined in the fit to the data. These values are invariably close to the q_z dependent σ_{eff} for the largest measured q_z in the data set being fitted.

F. Grazing incidence diffraction and Bragg rods

X-ray grazing incidence diffraction experiments were performed to probe the in-plane structure of the free surface of the alkane melt [36]. Here, the incident angle was set to be less than the critical angle α_c. Thus the incident x-rays experience total external reflection and only evanescent waves penetrate the surface to a depth of $\sim 1/\sqrt{q_c^2-q_z^2}\approx 100$ Å. In this configuration, the intensity of x-rays scattered by the surface is enhanced while that scattered by the bulk is reduced. By scanning the detector angle θ_D out of the plane of specular reflection, the scattered intensity is measured as a function of the in-plane component q_r of the wave-vector transfer [36,37] (Fig. 3). The use of Soller slits yields a sharp in-plane resolution of $\Delta q_r\approx 0.015$ Å^{-1} full width at half maximum (FWHM), while allowing the collection of rays scattered from a large sample surface area. In measuring the integrated intensity as a function of q_r, the vertical detector slits have been opened up to 25 mm, allowing signal integration over a range in q_z of 0.25 Å^{-1}. The orientation of the molecular chains can be further probed by measuring the scattered intensity distribution along q_z at the in-plane diffraction peak positions, the so called Bragg rods. A vertically oriented metal wire Braun linear position sensitive detector (PSD) was employed to measure this distribution.

The q_r peak positions yield information on the average molecular chain spacing projected on the surface and the peak width is related to the correlation length in the ordered crystalline phase. Loss of positional order may result through a finite crystallite size, proliferation of crystal defects or hexaticlike loss of positional correlation. The signatures of these different causes in the diffraction patterns are almost identical and it is only possible to separate these effects by very high resolution line shape measurements which are not practical with the present experimental setup.

The intensity distribution along q_z is determined by the product of the molecular form factor and the structure factor.

The equal-intensity contours of the form factor for an elongated chain molecule are pancake shaped, lying normal to the chain axis; and the structure factor of a hexagonal monolayer consists of lines parallel with q_z and arranged on hexagonal lattice sites [36–38]. When the chains tilt, the form factor tilts also, but the structure factor is unaffected if the lattice does not distort. Thus the q_z dependence of the in-plane peak intensity, determined by the intersection between the ''pancake'' and the vertical lines, will vary in a characteristic way with the azimuthal direction and magnitude of the tilt [36–38].

More quantitatively, we denote by Q_z (or Q_r) the wave-vector component along (or normal to) the *molecular axis*, and by q_z(or q_r) that along (or normal to) the *surface normal*. The form factor of a cylindrical electron distribution with diameter a and height d, a good approximation for alkane chains in the rotator phases, is then given by $F(Q_r,Q_z)=f(Q_zd)\times g(Q_ra)$, where $f(Q_zd)=\sin(Q_zd/2)/(Q_zd/2)$, $g(Q_ra)=J_1(Q_ra)/(Q_ra)$, and J_1 is the first order Bessel function. For alkane chains of $a\approx 5$ Å, $g(Q_ra)$ is monotonically decreasing in the Q_r range to be discussed whereas $f(Q_zd)$ has its maximum at $Q_z=0$ and a width of $2\pi/d$. For a tilt angle θ away from the surface normal [36,38], the Q and q components are related by

$$Q_z=q_z\cos\theta-q_x\sin\theta, \tag{9}$$

$$Q_r=\sqrt{q_y^2+(q_z\sin\theta+q_x\cos\theta)^2}, \tag{10}$$

with $q_x=|G_{hk}|\cos\psi_{hk}$ and $q_y=|G_{hk}|\sin\psi_{hk}$, $\vec{G}_{hk}$ being the reciprocal lattice point considered and ψ_{hk} is the angle from the tilt direction to $\vec{q}_r=\vec{G}_{hk}$. The form factor $|F(Q_r,Q_z)|^2\propto|f(Q_z)|^2$ is peaked at $Q_z=0$, or equivalently at $q_z=|G_{hk}|\tan\theta\cos\psi_{hk}$.

Multiplying the form factor by the structure factor of an hexagonally packed monolayer, the scattered intensity is given by [36]

$$I(q_z)\propto\left[\left(\frac{\sin(Q_zd/2)}{Q_zd/2}\right)^2 e^{-(Q_z\sigma_0)^2}\right]e^{-(q_z\sigma_z)^2}|T(\alpha)|^2|T(\beta)|^2. \tag{11}$$

Here $\exp(-(Q_z\sigma_0)^2)$ represents the gradual decrease of the electron density of the molecule at its two ends, $\exp(-(q_z\sigma_z)^2)$ is due to the surface roughness, and $|T(\alpha)|^2=|2\sin\alpha/(\sin\alpha+\sqrt{\cos^2\alpha_c-\cos^2\alpha})|^2$ is the surface enhancement factor [39], which is about 4 at $\alpha\approx\alpha_c$ and approaches unity for $\alpha\gg\alpha_c$. $|T(\beta)|^2$ is the corresponding term for the reflection angle β and has the same form.

When the molecules are normal to the surface, $Q_z=q_z$ and $Q_r=q_r$. Consequently the form factor $|F(Q_r,Q_z)|^2\propto|f(Q_z)|^2=|f(q_z)|^2$ has its maximum at $q_z=0$. The six lowest-order in-plane reflections of an hexagonal lattice $\vec{G}_{(\pm1,0)},\vec{G}_{(0,\pm1)},\vec{G}_{(\mp1,\pm1)}$ (where $\vec{G}_{(1,0)}$ and $\vec{G}_{(0,1)}$ are the primitive reciprocal lattice vectors) have identical rods and in-plane peak positions. The Bragg rod is characterized by a sharp peak at $q_z=q_c$ on top of a broad peak with its maximum at $q_z=0$, the sharp peak being due to the enhancement of the broad peak at the critical angle, and the broad peak coming from the molecule's form factor.

When the molecules are tilted, the degeneracy among the six lowest-order Bragg rods is lifted. Often the molecules tilt towards the most symmetric directions, either towards the nearest neighbors, or towards the next-nearest neighbors. When molecules tilt towards the nearest neighbors, two peaks result: one at $q_z=0$ for $\vec{G}_{(\pm1,0)}$, and another at $q_z=G_{(0,1)}\tan\theta\cos30°>0$ for $\vec{G}_{(0,1)}$ and $\vec{G}_{(-1,1)}$. The peaks at negative q_z cannot be observed. Conversely, the tilt angle θ can be calculated from peak coordinates (q_r,q_z):$\tan\theta=q_z/(q_r\cos30°)$. Both peaks can be fitted quantitatively with the same parameters d, θ, σ_0, σ_z. Note that for the peak at $q_z=0$, $q_x=G_{(\pm1,0)}\cos90°=0$ and $q_y=G_{(\pm1,0)}\sin90°=G_{(\pm1,0)}$; and for the peak at $q_z>0$, $q_x=G_{(0,1)}\cos30°$ and $q_y=G_{(0,1)}\sin30°$.

When molecules tilt towards the next-nearest neighbors, two peaks can be observed as well: one at $q_z=|G_{hk}|\cos60°\tan\theta=\frac{1}{2}|G_{hk}|\tan\theta$ for $\vec{G}_{(1,0)}$ and $\vec{G}_{(-1,1)}$, and another one at $q_z=|G_{hk}|\tan\theta$ for $\vec{G}_{(0,1)}$. This tilt direction is characterized, therefore, by the q_z of one peak being twice that of the other, with no peak at $q_z=0$. The tilt angle θ can be calculated, again, from the peak coordinates (q_r,q_z) of the two peaks. Both peaks can be fitted quantitatively, again, with the same set of parameters $d,\theta,\sigma_0,\sigma_z$. Note that for the peak at larger q_z, $q_x=G_{(0,1)}\cos0°=G_{(0,1)}$, and $q_y=G_{(\pm1,0)}\sin0°=0$; and for the peak at smaller q_z, $q_x=G_{(1,0)}\cos60°$, $q_y=G_{(1,0)}\sin60°$.

Finally, it should be noted that when the sample is powderlike, rather than a single crystal, and the molecules are tilted but to an extent which leaves the in-plane peak positions unresolved, the measured intensity along the q_z direction will be a superposition of two (or more) of the individual Bragg rod patterns discussed above. Nevertheless, it is possible to identify the molecular tilt and its direction from the superimposed patterns as we show below.

G. Surface tension

We have also studied the thermodynamics of the n-alkane surfaces by measuring the surface tension with the Wilhelmy plate method [26]. The liquid completely wets the Wilhelmy plate, a roughened thin platinum plate in our experiment, and pulls it downward. The force exerted on the plate is measured by an electronic balance. The surface tension is simply this force divided by the circumference of the plate's cross section which is, in practice, twice the plate width. One can check the complete wettability of the plate by observing the meniscus. Plates made of materials other than platinum perform equally well, as long as they do not contaminate the liquid and are completely wet by the liquids to achieve a zero contact angle. Results obtained using a filter paper plate were indistinguishable from those obtained using a platinum plate. However, since a platinum plate can be easily cleaned by flaming with a torch, the same plate can be used repeatedly thus eliminating experimental errors due to circumference variation from one paper plate to another.

The samples were contained in a temperature regulated cell, as described in Sec. II A above. The temperature is changed at a rate slow enough so that further rate reduction yields identical results. Typically, a data point is measured every 30 sec while the temperature is varied at a rate

$\leqslant 0.3$ m°C sec^{-1}. Except for the region near the bulk freezing (or melting) temperature, the results are independent of the direction in which the temperature is varied.

The surface tension γ is a direct measure of the surface excess free energy [26]

$$\gamma = \epsilon_s - \epsilon_b - T(S_s - S_b), \tag{12}$$

where ϵ_s and ϵ_b are the energies and S_s and S_b the entropies for the surface and the bulk, respectively. The temperature slope of surface tension yields information on the surface excess entropy: $d\gamma/dT = -(S_s - S_b)$, which are directly related to the ordering and disordering of the molecules on the surface. For ordinary liquid surfaces, the molecules on the surfaces are less constrained than those in the bulk, thus S_s is slightly larger than S_b, yielding $d\gamma/dT < 0$. A negative temperature slope has been indeed observed for all the simple liquid surfaces. Any ordering on the liquid surface results in a reduction of the surface entropy S_s, resulting in $d\gamma/dT > 0$. A slope change indicates, therefore, an ordering transition at the surface. Such slope changes have been observed in liquid metals [40], sodium dodecyl sulphate solutions [41], and Langmuir films [24,25]. When the surface freezing occurs via a first-order transition, the slope of the surface tension should change abruptly from a small negative value in the higher temperature liquid surface phase to a large positive value in the lower temperature crystalline surface phase. This effect was indeed observed in alkanes, as shown in Sec. III.

III. RESULTS AND DISCUSSION

A. The liquid surface phase

At temperatures higher than ~ 3 °C above the bulk freezing temperatures T_f, the reflectivity of liquid alkane surfaces has the smoothly decreasing shape typical of ordinary liquid surfaces, and given in Eq. (8). This indicates a capillary-wave-broadened density profile which increases smoothly and monotonically from a zero density on the vapor side to the bulk liquid density on the liquid side. In Fig. 4 we show in circles the reflectivity curves measured at $T > T_s$ for C_{20}, C_{30}, and C_{44}. The solid lines in the figure show the excellent fits to the capillary wave form of Eq. (8). An effective roughness of $\sigma_{\text{eff}} \approx 4.4$ Å is found to account reasonably well for all alkanes at temperatures just above the formation of the monolayer. Since $\sigma_{\text{eff}}^2 = \sigma_0^2 + \sigma_{\text{cw}}^2$ where the last term is the capillary wave contribution in Eq. (7), the capillary wave contributions to surface roughness of two different liquids should have the ratio

$$\sigma_{cw,1}/\sigma_{cw,2} \approx \sqrt{\gamma_2/\gamma_1} \tag{13}$$

where the weak logarithmic dependences on the molecular size and the experimental resolution makes the small differences between these two liquids negligible in Eq. (7). Since σ_0 originates in the atomic form factor which has a similar extent for carbon and oxygen, we can use the alkane measured [35] $\sigma_0 = 1.1$ Å for both alkanes and water. Employing now the measured [35] $\sigma_{\text{eff}}^{\text{alkanes}} \approx 4.4$ Å and [42] $\sigma_{\text{eff}}^{\text{water}} = 2.7$ Å, we obtain $\sigma_{\text{cw,alkane}}/\sigma_{\text{cw,water}} = 1.7$, in good agreement with $(\gamma_{\text{water}}/\gamma_{\text{alkane}})^{1/2} = 1.6$, obtained from the measured [42] $\gamma_{\text{water}} = 72$ mN/m and our $\gamma_{\text{alkane}} = 28$ mN/m.

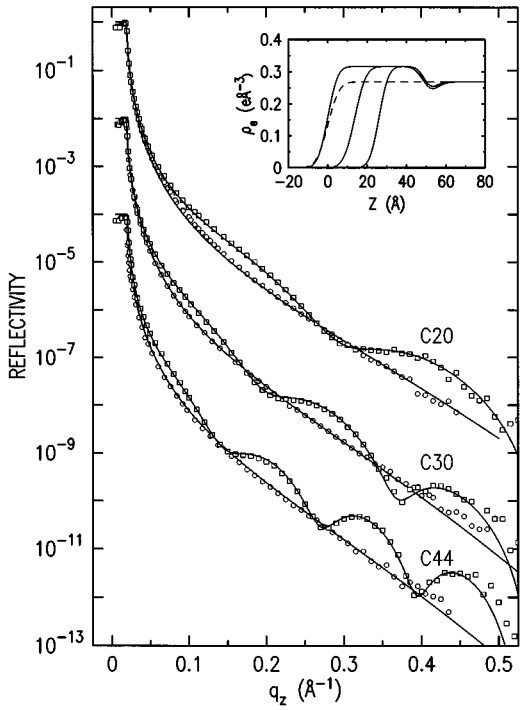

FIG. 4. The reflectivities of C_{20}, C_{30}, and C_{44} surfaces in their liquid state at high temperatures (circles) and at the crystalline phase at the lower temperatures (square). The lines are the model fits discussed in the text. The corresponding electron densities in the crystalline (solid) and liquid (dashed) surface phases are shown in the inset.

We conclude therefore that at temperatures above the formation of the monolayer, the surface roughness behaves as that of simple liquids and is dominated by capillary wave contributions.

B. The crystalline surface phase

For n alkanes of $16 \leqslant n \leqslant 50$, there exist a temperature range ΔT immediately above the bulk freezing temperature T_f, within which the surface crystalline layer is thermodynamically stable. This layer is formed via a first-order phase transition at $T_s = T_f + \Delta T$. This transition can be conveniently monitored by measuring the reflected intensity at a particular q_z, say $q_z = 0.2$ Å^{-1}, as a function of the temperature, as shown in Fig. 5(a). The first order transition to the crystalline monolayer is clearly visible as the intensity jumps abruptly from that of the liquid surface to that of the crystalline surface phase. For $T_f \leqslant T \leqslant T_s$ the intensity remains constant, indicating that no further changes occur in the surface crystalline layer, either in thickness or in density. The reflected intensity drops to virtually zero at the bulk freezing point where the surface becomes macroscopically rough.

The results of the x-ray and surface tension measurements on the crystalline surface phase for all chain lengths studied are summarized in Table I. In the following we discuss the various features of the surface monolayer emerging from these measurements.

1. Crystalline monolayer thickness

The formation of the surface crystalline layer is clearly seen by the appearance of the pronounced modulations in the

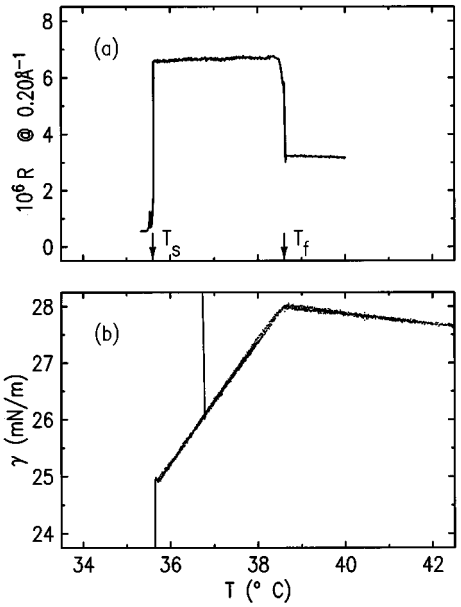

FIG. 5. The temperature dependence of (a) the reflectivity at a fixed q_z and (b) the surface tension for C_{20}. The first order transition, in which the crystalline monolayer is formed at the surface at $T=T_s$, is clearly visible as a sharp intensity jump in (a) and abrupt slope change in (b). T_f marks the bulk freezing point.

x-ray reflectivities shown in Fig. 4. The solid lines are fits based on a two-slab model discussed below, and the inset displays the resultant density profiles for the three alkanes.

The simplest model for the density profile of this layer is a single slab of thickness D and a density $\rho \neq \rho_l$, where ρ_l is the electron density of the bulk liquid. The modulation period is $\Delta q = 2\pi/D$ and the amplitude is determined by $\rho - \rho_l$. Two interfacial widths σ_1 and σ_2, representing the vapor and liquid interfaces, respectively, are also included in the model. The calculated reflectivity normalized to the Fresnel reflectivity, shown in a dash line in Fig. 6 for C_{44}, provides a reasonably good agreement with the data. The corresponding density profile obtained from the fit is shown as the dashed line in the inset of Fig. 6. The surface layer density, 0.321 e/Å^3, is found to be 20% higher than that of the bulk liquid alkane and is similar to the density of the $(CH_2)_{n-2}$ segment in the rotator phases [1]. The fitted D value obtained is about 2 Å shorter than the corresponding fully extended molecular length, calculated using the literature value of 1.27 Å per bond [1]. This reduction in D is consistent with the molecular tilt of $\sim 14°$ observed for this molecule in the surface layer.

Even though it captures the essence of the modulations in the reflectivity, this one-slab model deviates from the experimental curve noticeably over large sections of the measured q_z range. This deviation becomes more obvious for data of large carbon numbers, as there are more modulations in a given q_z range. We propose, therefore, a more realistic model, which takes into account the reduced density of the CH_3 group by adding a lower density slab at the crystalline layer-liquid interface. A similar layer at the vapor interface is absorbed into the surface roughness parameter σ_1. This depletion zone is characterized by its density $\delta\rho$, the zone width δD and the interfacial width σ for its two interfaces. Since the range of the data, and the consequent real space resolution, are insufficient to determine $\delta\rho$ and δD independently, we typically fix δD at a value of 2.27 Å (the nominal size of a CH_3 group) and vary only $\delta\rho$ and σ. Thus, this model has five independent variables: the thickness D and the density ρ for the $CH_3(CH_2)_{n-2}$ layer, the density $\delta\rho$ and the interfacial width σ of the depletion zone and the vapor-layer interface width σ_1. The density of the liquid bulk is fixed at the literature value of 0.269 eÅ^{-3}, which is consistent with the critical angle value observed in the reflectivity data. With this two-slab model, reflectivities of all carbon number alkanes are well fitted over the entire q_z range, as shown for C_{44} by the solid line in Fig. 6.

The fitted density ρ of the $CH_3(CH_2)_{n-2}$ slab is practically identical for all carbon numbers: 0.317 ± 0.05 eÅ^{-3}. This is about 18% higher than the liquid bulk value. This value is also consistent with data measured by grazing incidence x-ray diffraction (GID), although a slight increase in density is found for $n \geq 44$, where a new surface phase is observed (see below). Using the area per molecule of $A \approx 20$ Å^2 (derived below from our GID measurements) and the 1.27 Å projected length of the eight electron CH_2 segment we obtain $\rho_{CH_2} = 8/(20 \times 1.27) = 0.315$ mN/m, in good agreement with the fitted value. The density $\delta\rho$ obtained from the fit for the depletion zone, with δD fixed at 2.27 Å, is 0.147 ± 0.03 eÅ^{-3}. As explained above, neither $\delta\rho$ nor δD can be determined independently in the fit. Rather, the difference of the areal density $(\delta\rho - \rho_{avg})\delta D$ is a well-defined quantity, where $\rho_{avg} = (0.317 + 0.269)/2 = 0.293$eÅ^{-3} is the average density, at the position of the depletion zone, in the absence of depletion, i.e., the mean of the densities of the bulk liquid and the $(CH_2)_{n-2}$ segment. This well-defined quantity can be used to estimate the actual length t of the CH_3 head group. By equating the *areal* density obtained from the fit, $(0.147 - 0.293)$eÅ$^{-3} \times 2.27$ Å with the calculated one, $(9/(tA) - 0.293\text{eÅ}^{-3}) \times t$ we obtain $t = 2.7 \pm 0.2$ Å, which is close to the ~ 3 Å head group length in the bulk crystal [43,44]. In the last expression, the first term in brackets is the areal density due to the nine electrons of the CH_3 group in a molecular area $A \approx 20$Å^2, and the second term is, again, the average areal density in the absence of depletion.

The layer thickness D variation with the carbon number n is shown in Fig. 7(a). It increases linearly with n, but has two slightly different slopes in two ranges. For $n \leq 30$, it increases as $D_{reflect} = (1.27n - 1.23)$ Å, very close to the calculated fully extended chain length $D_{calc} = 1.27(n-1)$ Å, where 1.27 Å is the projection of a C—C bond length on the chain axis. This agreement indicates that the chains are fully extended and oriented normal to the liquid surface. For $n > 30$, the thickness varies as $D_{reflect} = (0.977n + 7.09)$ Å. The smaller slope indicates that either the chains are not fully extended, or that they are tilted away from the normal. From the reflectivity data alone, these two possibilities can not be resolved. However, if we do assume fully extended molecular chains tilted by an angle θ away from the surface normal, θ can be calculated from $\cos\theta = D_{reflect}/D_{calc}$. The tilt angles θ so calculated for all chain lengths are shown in Fig. 7(b). As can be seen, $\theta \approx 0$ for $n < 30$, thereafter increasing monotonically, but nonlinearly, to $\sim 23°$ for C_{44}. As

TABLE I. Experimental results of the x-ray and surface tension measurements for all chain lengths studied. n is the carbon number, D is the layer thickness measured by x-ray reflectivity, q_r is the position of in-plane grazing incidence diffraction peak, and q_z is the peaks of the corresponding Bragg rods. The bulk freezing point, T_f, and the temperature range of existence ΔT of the surface crystalline phase were derived from the x-ray and surface tension measurements independently. δ is the distortion parameter, discussed in the text, A is the area per molecule. The entropy change upon formation of the surface layer, ΔS_s is equal to, and was calculated from, the slope difference of the surface tension below and above the layer formation temperature T_s. The corresponding bulk value, ΔS_b, was obtained from the published values for bulk rotator phases [1,57].

n	D (Å)	q_r (Å^{-1})	q_z (Å^{-1})	T_f (°C)	ΔT (°C)	δ	A (Å^2)	ΔS_s (mN m^{-1}K^{-1})	ΔS_b (mN m^{-1}K^{-1})
14				4.50	0.00				
16				17.69	1.20			0.896	1.16
17				24.00	2.12			0.943	1.14
18	21.66	1.524		29.33	2.05	0.000	19.63	1.00	1.27
19				34.40	2.66			1.12	1.25
20	24.11	1.519	0.0	38.65	2.97	0.000	19.76	1.16	1.28
21	25.49	1.517	0.0	41.93	2.67	0.000	19.81	1.23	1.30
22	26.75	1.524		46.25	3.13	0.000	19.63	1.29	1.42
23	28.22	1.521		50.00	3.11	0.000	19.70	1.32	1.42
24	29.45			52.91	2.98			1.39	1.50
25				55.83	3.10			1.45	1.50
26	31.67	1.520		58.44	2.99	0.000	19.73	1.51	1.52
28				63.40	2.96			1.64	1.62
30	36.63	1.516		67.56	2.82	0.005	19.73	1.72	
32	38.43	1.510		70.69	2.52			1.76	
36	42.00	1.496	0.0	76.94	2.48	0.045	19.50	1.94	2.05
			0.392						
40	46.15	1.489		81.70	2.30			2.11	
44	50.34	1.476	0.356	85.70	1.30	0.106	18.71	3.02	3.45
			0.740						
46	49.1			88.05	0.55			3.29	
50				91.10	0.40			3.17	3.76

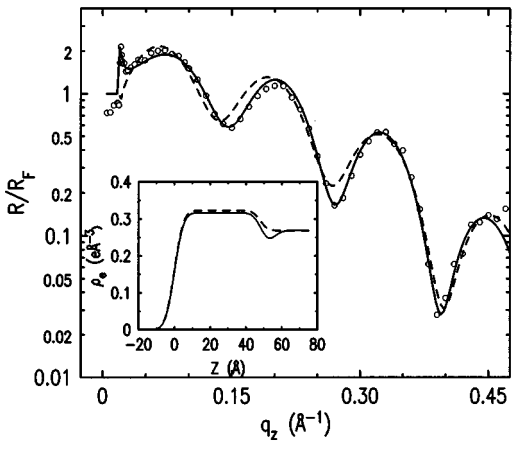

FIG. 6. R/R_F for C_{44}. The circles are the experimental data, the solid and dashed lines are the best fits of two different density models shown in the inset. The one in the solid line is a two-slab model taking account of the density depletion at the chain ends due to the less dense CH_3 groups. The dashed line results from a single slab representation of the monolayer. The more realistic two-slab model clearly agrees better with the measurements.

discussed below, the Bragg-rod measurements for $n=20$, 36, and 44 are consistent with this calculation, thus supporting the scenario of a rigid molecular tilt over that of a molecular conformational change.

2. In-plane order

The in-plane order in the monolayer was determined by GID measurements. In the high temperature liquid surface phase, the scattering intensity drops monotonically for increasing q_r. The structure factor for the liquid *surface* was too weak to be detected [45]. The scattering from *bulk* liquid displays a broad peak at $q_r=1.35$ Å^{-1}, having a width (FWHM) of $\Delta q_r \approx 0.35$ Å^{-1} for C_{20}, which yields a correlation range of a few molecules [46]. The formation of the crystalline surface monolayer at T_s, is marked by the appearance of a sharp peak at $q_r \approx 1.52$ Å^{-1}, as shown in Figs. 8(a)–8(c) for C_{20}, C_{36}, and C_{44}. This Bragg peak clearly originates from long range positional order in the densely packed surface layer [47]. Within our resolution of $\Delta q_r = 0.015$ Å^{-1}, neither the peak position nor the peak width change with temperature over the ~ 3 °C range down to T_f. The thermal expansion coefficient calculated from the uncertainty in the peak position is, therefore, less than 3×10^{-3} °C^{-1}, and the correlation length is temperature independent. The thermal expansion coefficient for the bulk

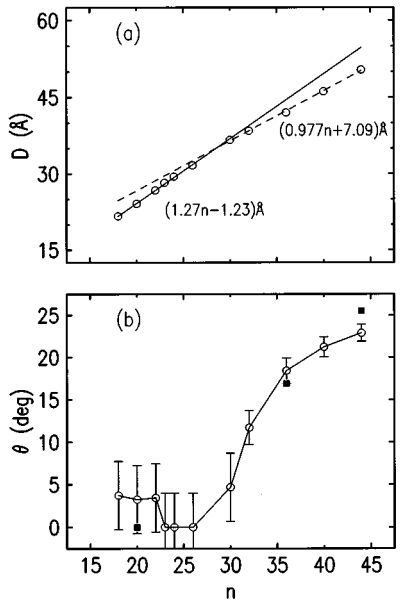

FIG. 7. (a) The thickness D of the surface crystalline layer, derived from the reflectivity measurements, as a function of the carbon number n. The two lines of two different slopes describe the data well for $n<30$ and $n>30$, respectively. (b) The molecular tilt angles from the vertical θ, deduced from D of (a) and the calculated, fully extended molecular lengths (circles). Independent Bragg rod measurements (open squares) agree well with these values.

hexagonal rotator phase [16] is $1\times10^{-3}\,^{\circ}\mathrm{C}^{-1}$, consistent with our results. For all chain lengths measured, the peak width is resolution limited at 0.015 $\mathrm{Å}^{-1}$ (Fig. 8), implying quasi-long-range order with a correlation length of at least 1000 Å. The mosaic distribution in the monolayer can be

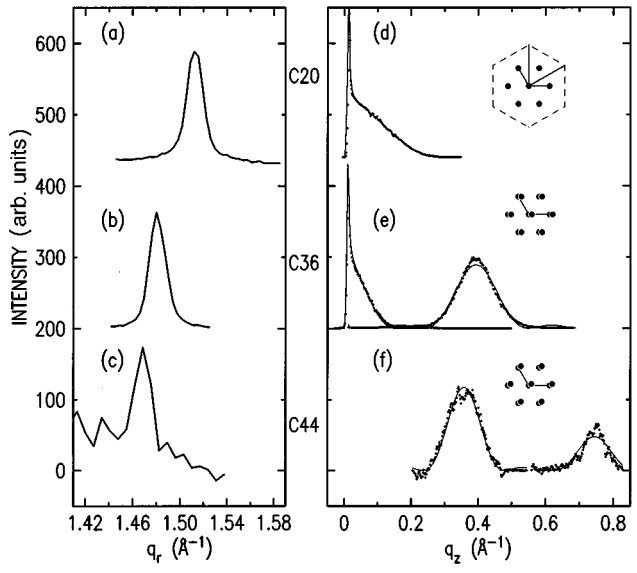

FIG. 8. (a)–(c) The in-plane GID peaks of the surface crystalline layer of C_{20}, C_{36}, and C_{44}, measured at $q_z=0$ $\mathrm{Å}^{-1}$ (a,b) and 0.35 $\mathrm{Å}^{-1}$ (c). (d)–(f) The corresponding q_z scans at the in-plane peak positions. The q_z scans indicate that the C_{20} molecules are normal to the surface (d), the C_{36} ones tilted towards their nearest neighbors (e), and the C_{44} ones tilted towards their next-nearest neighbors (f), as shown in the insets.

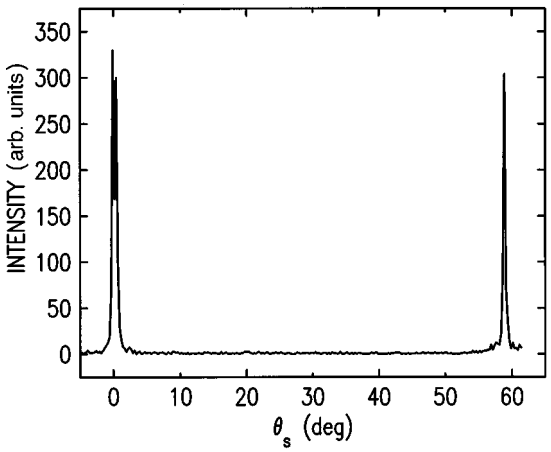

FIG. 9. The intensity variation of the $q_z=0\mathrm{Å}^{-1}$ GID Bragg peak of the crystalline surface monolayer of C_{40} upon a sample rotation θ_s (see geometry in Fig. 3). The sharp peaks 60° apart indicate a single very large crystallite (of lateral ~mm dimensions) with hexagonal symmetry.

observed directly by measuring the intensity at the q_r peak position as a function of the sample azimuthal rotation θ_s as shown in Fig. 3. If the 2D ''powder'' comprising the monolayer is fine, with many small crystallites, an intensity independent of the sample rotation would be obtained, while for a coarse ''powder'' made of a few large crystals, discrete peaks would be observed upon sample rotation. Indeed, the measured intensity displays discrete peaks in groups ~60° apart in θ_s, as shown in Fig. 9, indicating (very few, if not a single) large crystal domains with six fold crystalline symmetry. Since the illuminated sample surface area is many mm^2, and the coverage is almost complete, the monolayer crystals must also have a similar area. Bearing in mind that the thickness of the crystals is only a few tens of Å, the aspect ratio of these crystals is amazingly large. In two-dimensions, thermal fluctuations are known to destroy true long-range positional order yielding quasi-long-range order. An experimental distinction between true- and quasi-long-range order would require very demanding high resolution line shape measurements, not currently available.

Note that our mm size crystallites are significantly larger than those of Langmuir films, where they are typically 100–1000 Å across. This can be understood by considering the coalescence energetics of small crystals into larger ones. In Langmuir films, the molecules are confined to the water surface, thus eliminating the possibility of removing domain walls through exchange of molecules with the bulk. This places an energy barrier on the coalescence of small crystallites into larger ones in Langmuir films. In alkanes, by contrast, the molecules on the surface are in full equilibrium with those in the bulk and free molecular exchange is allowed. Apparently, this lowers considerably the energy barriers on the elimination of domain boundaries and on the coalescence of small crystallites into large ones.

Returning now to Figs. 8(a)–8(c) and 10(a), we note that for all samples with $n<30$ the in-plane peak is nearly fixed at $q_{r0}=1.52\mathrm{Å}^{-1}$, i.e., the lattice plane spacing is 4.13 Å and the chain-chain spacing is $(2/\sqrt{3})4.13=4.77$ Å. Assuming hexagonal packing for our monolayer, the area per chain is $2\times4.13^2\tan30^{\circ}=19.7\mathrm{Å}^2$. This value is consistent with that

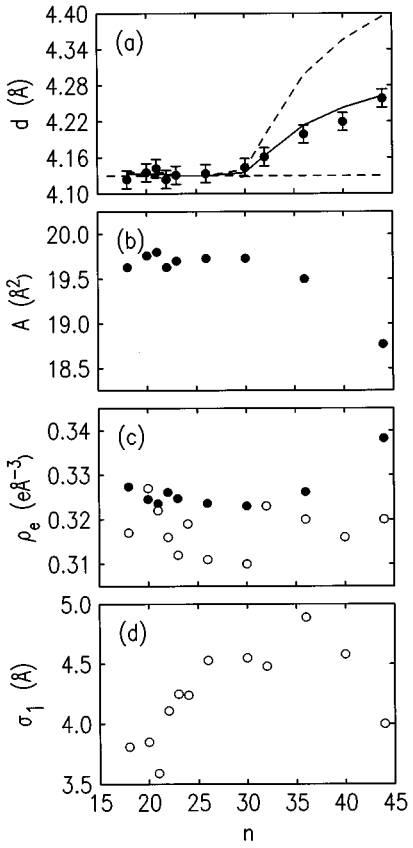

FIG. 10. (a) The measured in-plane lattice spacings d (closed circles), derived from the q_r positions of the $q_z=0$ Å^{-1} peaks, except for C_{44}, where it is derived from the $q_z=0.35$ Å^{-1} peak, since there is no $q_z=0$ one. For $n>30$ the tilt towards nearest neighbors (without distorting the hexagonal packing in the axis-normal plane) should result in the distortion of the in-plane hexagonal packing, yielding two distinct spacings. The dashed lines are these hypothetical spacings based on the tilt angle calculated from the reflectivity measurements, Fig. 7, assuming $\delta=0$. The single spacing observed for each n in the actual measurements takes the average of the two values. (b) The area per molecule in the plane perpendicular to the molecule's axis. (c) The electron densities, as deduced from the GID measurements (closed circles) and the reflectivity measurements (open circles). (d) The surface roughness parameter σ_1 obtained from the fits to the measured reflectivities. Note the gradual increase with n for $n<44$ and the abrupt decrease for the new solid phase at $n=44$. Similar abrupt changes are observed in A and ρ_e at the same position in (b) and (c), respectively.

of the bulk rotator R_{II} phase [4,5], where the molecules are, on average, oriented normal to the layer and packed hexagonally. For $n>30$, the peak position q_r decreases, indicating that the in-plane spacing increases, with the carbon number n. Assuming rigid molecules, this is indicative of a molecular tilt. The tilt direction for $30<n<44$, according to the C_{36} Bragg-rod measurements discussed below, is towards nearest neighbors. If we assume that the molecules tilt as rigid cylinders and stay in contact, this tilt direction should distort the in-plane hexagonal packing in a characteristic way, and, as discussed in Sec. II F, should split the sixfold-degenerate in-plane peak into two: a twofold-degenerate one at $q_{r1}=q_{r0}$ and a fourfold-degenerate one at $q_{r2}=q_{r0}\cos\theta$, where θ is the tilt angle. Using now the tilt angles derived from the reflectivity data and given in Fig. 7 the values of q_{r1} and q_{r2}, and the corresponding in-plane spacings d_1 and d_2 can be calculated. The spacings are plotted as dashed lines in Fig. 10(a). As can be seen from the error bars, the difference between the calculated d_1 and d_2 and, hence, also between the calculated q_{r1} and q_{r2}, is well beyond the experimental resolution. Nevertheless, only a *single* $q_z=0$ diffraction peak could be observed experimentally for all chain lengths taking, interestingly, the average of the two estimated values, shown by the solid line in Fig. 10 (a). Thus, the assumption that the molecules stay in contact, with circular cross sections, when tilted is untenable, since this should have yielded two peaks, one at $(q_{r1}=q_{r0},q_z=0)$ and the other at $(q_{r2}<q_{r1},q_z>0)$. The observations of a single q_r peak position and a molecular tilt towards nearest neighbors, can still be reconciled if upon tilting the in-plane lattice stays hexagonal, but the lattice spacing expands commensurately with the tilt. In this case we should observe two peaks: one at $(q_{r1}<q_{r0},q_z=0)$ and another at $(q_{r2}\approx q_{r1},q_z>0)$, i.e., both peaks have the same in-plane position but different plane-normal positions. This is indeed the GID pattern observed for C_{36}, as discussed below. Note, however, that the C_{36} data does not dictate a strict in-plane hexagonal symmetry. In fact, any coupling between the tilt and the lattice would result in breaking this in-plane symmetry. Rather, an approximate one, with two in-plane peaks at a separation smaller than the experimental resolution is still supportable by the data. We favor this ''expanding hexagon'' model for all chain lengths on the strength of the C_{36} and C_{44} q_z-resolved GID data and the single (q_z-unresolved) in-plane peaks observed for all other chain lengths. However, since no q_z-resolved measurements are available for other lengths, significant distortions from a near-hexagonal in-plane packing can not be ruled out for tilted chains other than $n=36$ and 44.

3. Molecular tilt

Both the direction and the magnitude of the molecular tilt can be determined from the q_z dependence of the intensity at the position of the peak in q_r, the so called Bragg rods, shown in Figs. 8(d)–8(f). Unlike the reflectivity, which provides a layer thickness averaged over both the crystalline and noncrystalline parts (if any) of the monolayer, from which the tilt magnitude can be extracted, assuming rigid, extended molecules, the Bragg rods result only from the crystalline parts of the monolayer. The Bragg-rods' width can be used to test the assumption of a rigid molecular tilt but most importantly, they allow an accurate determination of the tilt *direction*, in addition to its magnitude. To unambiguously determine this structure, the (q_r,q_z) peak positions must be found for all the low-order peaks. The measured positions are shown in Table I. The in-plane spacings $d=2\pi/q_r$, corresponding to the Bragg peaks occurring at $q_z=0$ Å^{-1} are plotted in Fig. 10(a). As discussed above, for hexagonally packed nontilted molecules, the six diffraction peaks are completely degenerate, and thus only one peak is observed in the 2D powder averaged q_z-q_r plane. The line shape is a product of a sharp surface enhancement spike at $q_z=q_c$ and a broad form factor distribution peaking at $q_z=0$Å^{-1}. The Bragg rods of the surface crystalline layer for $n\leqslant 30$ display all these features, as shown in Figs. 8(a),8(d). We conclude,

therefore, that the molecules in the monolayer are normal to the surface, consistent with the reflectivity measurements. Quantitatively the Bragg rods can be described by Eqs. (1) and (2) and (9)–(11), noting that $Q_z = q_z$ and $Q_r = q_r$. Specifically, as shown in Fig. 8 (d), C_{20} can be well fitted yielding a molecular length of $d = (22 \pm 1.0)$ Å, close to, but ~ 2 Å shorter than the reflectivity result.

For $30 < n < 44$, the 2D powder average yields two doubly degenerate peaks, at $q_z = 0$ and a finite positive q_z, indicating that the molecules are tilted towards their nearest neighbors. The doubly degenerate peak at negative q_z is not accessible in this experimental geometry. The scans for C_{36} are shown in Fig. 8(e). Within our experimental resolution, these two peaks in q_z for C_{36} have the same in-plane position q_r, indicating an hexagonal projection on the surface, but a distorted projection when viewed along the chain axis. Substituting the proper relations for a nearest-neighbor tilt into Eqs. (9)–(11), both peaks can be fitted quantitatively, as shown in a solid line in Fig. 8(e), for C_{36}. This fit yields $d = 46$ Å, which coincides with the calculated 46 Å length of the fully extended molecule, and a tilt of $\theta = 17.6°$, consistent, again, with the reflectivity data shown in Fig. 7(b).

For $n \geqslant 44$, the powder average yields two peaks. A doubly degenerate one at some $q_z = q_{z1} > 0$ and a singly degenerate one at $q_{z2} = 2q_{z1}$, indicating that the molecules are now tilted towards the next-nearest neighbors. For C_{44}, the in-plane positions q_r of these two peaks are the same, $q_r = 1.48$ Å^{-1}, indicating, again, an undistorted hexagonal projection on the surface and a distorted projection normal to the chain axis. The tilt angle θ can be determined from the coordinates of the peaks (q_{r1}, q_{z1}) and (q_{r2}, q_{z2}), as $\tan\theta = q_{z1}/(q_{r1}\cos 60°) = q_{z2}/q_{r2}$. Substituting into Eqs. (9)–(11) the proper relations for the next-nearest neighbor tilt, both peaks can be fitted quantitatively, yielding $d = 50$ Å for C_{44}, which is consistent with the reflectivity results of Fig. 7(a) though somewhat shorter than the 54.6 Å length calculated assuming a fully extended molecule, and $\theta = 26°$, which is, again, consistent with the reflectivity data shown in Fig. 7(b).

The transition from untilted to tilted molecules with increasing chain length can perhaps be understood by considering the increased molecular diameter at the chain ends [15]. Spectroscopic measurements [48,49] clearly show that there are substantial numbers of gauche-bond defects predominantly near the chain ends in the rotator phases. The number of these defects increase with increasing temperature and thus they play a larger role in longer chain alkanes, the melting temperatures of which are higher than those of shorter chains. When averaged over their individual configurations, these *gauche* defects will result in larger effective widths at the ends of the molecules as compared to that at their centers. This was also confirmed by scanning tunneling microscopy (STM) measurements [50] of alkanes adsorbed on graphite. Consider, therefore, a monolayer consisting of closely packed dumbbell-shaped molecules. The intermolecular distance is determined by the larger widths of the ends, w_{end}, thus leaving the distance between the $(CH_2)_{n-2}$ segments larger than their diameter. Simple geometry shows that a tilt from the vertical by an angle θ decreases the distance between adjacent $(CH_2)_{n-2}$ segments as $w_{\mathrm{end}}\cos\theta$, but at the same time reduces the lengthwise overlap between adjacent segment by $2w_{\mathrm{end}}\sin\theta$. For short chains the usual energy-entropy balance in the monolayer favors a vertical orientation for the molecules. However, as n increases, the attraction between adjacent $(CH_2)_{n-2}$ segments also increases. Above some limit, it will become sufficient to offset the balance and the molecules will seek a reduction of the distance between adjacent $(CH_2)_{n-2}$ segments by tilting. A tilt, however, reduces the overlap, and thus the attraction as well. A new balance of the free energy will, therefore, be obtained for some finite tilt angle θ.

A tilt direction transition, where no other parameter varies (i.e., tilt magnitude, distortion, and area) is energetically very subtle [51], so that different tilt directions in the bulk and at the surface, while not understood in detail, are not too surprising. In fact, the bulk phase diagram shows also another rotator phase (the R_{III}) where the tilt is intermediate between nearest neighbors and next-nearest neighbors. Thus, the tilt direction transition may occur, in the scenario above, as a result of the (somewhat more subtle) influence of the free volume obtained for the longer chains.

According to the reasoning above, the tilt direction and angle must be a balance of entropy, which is a function of k_bT, and energy, which varies with chain length and tilt directions. Thus, the balance should be, in principle, temperature dependent and so should be the tilt direction and angle. The temperature range of existence of the surface phase in alkanes is, however, too small to allow the necessary temperature variation, and the bulk freezing point is reached before a tilt transition, or a direction transition, can be affected. In alkane mixtures, however, the bulk freezing point can be tuned by varying the bulk composition. The bulk freezing temperatures of C_{26}/C_{36} mixtures were found, indeed, to be greatly depressed relative to that of pure C_{36} melt. The surface crystalline monolayer of pure C_{36} that was observed to form on the liquid bulk of the mixtures could indeed be tuned, for a particular (rather narrow) composition range, to go through a first order transition from a rotator phase with a nearest neighbor tilt direction to a crystal phase with a next-nearest neighbor tilt direction by lowering the temperature [9].

C. Surface phase behavior

Using the in-plane (q_r, q_z) peak positions we can compute [17] the area per molecule (A) viewed normal to the chain axis and the distortion (δ) both of which are listed in Table I. It is easy to show that $\delta = \left|1 - \sqrt{[(2q_a/q_b)^2 - 1]/3}\right|$ and $A = 8\pi^2/(q_b\sqrt{4q_a^2 - q_b^2})$, where $q = \sqrt{q_r^2 + q_z^2}$ and the subscript a refers to the peak with the lower (higher) q_z for the next-nearest-neighbor (nearest-neighbor) tilt direction for C_{44} (C_{36}) and b to the other peak. In the A values plotted in Fig. 10(b), we see that for $n < 44$ we have $A \approx 19.65$ Å^2, including the tilted C_{36} phase. This is consistent with the values of the bulk rotator phases. For C_{44}, however, A appears to have taken a discontinuous jump to a lower value of 18.71 Å^2. This value, which is consistent with a transition from a rotator to a nonrotator crystal phase in the bulk, provides a clue to the nature of the transition in the surface phase at $n \approx 44$. In the untilted hexagonal phase $\delta = 0$. In the tilted phase of C_{36} we find $\delta = 0.045$, which is consistent with the low values observed for δ in the R_{IV} bulk

rotator phase where the distortion is induced by the tilt [17]. The high temperature bulk rotator phase of C_{33}, for example, has [17] $A=19.7$ Å^2, $\delta=0.045$ and $\theta=19°$. An important distinction between the surface and bulk rotator phases is the direction of the tilt. While the area and distortion magnitude are the same, in the bulk rotator phases the tilt is either towards next-nearest neighbors or at intermediate positions, while the surface rotator phase has a tilt towards nearest neighbors.

For the tilted phase of C_{44} we compute $A=18.71$ Å^2 and $\delta=0.106$, which we compare with the nonrotator crystal phases of the corresponding long chain alkanes [52] where C_{40} and C_{44} have $A=19.23$ and 19.17 Å^2, $\delta=0.101$ and 0.106 and $\theta=20.6°$ and 22.7°, respectively. It is thus clear that the transition between the two tilted surface phases at $n\approx44$ is a rotator to crystal phase transition. Furthermore, the in-plane peak positions provide yet another way of computing the electron density of the surface crystalline layer, which can be compared with the values determined from the reflectivity data fits. With eight electrons per CH_2 group and a length, along the chain, of 1.27 Å, the electron density is just $8/(1.27A)$ eÅ^{-3}, where A is the area per molecule as viewed along the molecular axis, and shown in Table I. The resultant densities are plotted in Fig. 10(c). As can be seen, for $n<44$ the GID data yields 0.320 e/Å^3 which is, within experimental error, equal to 0.317 e/Å^3 determined from the reflectivity fits. For C_{44}, however, a higher electron density of 0.333 e/Å^3 is obtained, consistent with the higher density of the crystal phase.

Another strong indication for a new phase for $n>44$ can be obtained from the n dependence of the surface roughness parameter σ_1. These values, as derived from the reflectivity fits for the lengths measured, are plotted in Fig. 10(d). While the accessible q_z range limits the accuracy of the fitted σ_1 values, a clear increasing trend with chain length is observed for $n<44$. However, for $n>44$, where the new phase comes in, a dramatic decrease in σ_1 is observed. The decrease in the observed σ_1 is very similar to that observed in Langmuir films upon compression of the monolayer from the 2D liquid to the 2D solid phase [53]. In that case it was shown that in the solid phase an extra damping of the capillary waves results from the nonzero bending rigidity constant K, as compared to the liquid phase where $K=0$ and the damping is due only to the surface tension γ. While a similar change of K upon the transition from a surface rotator to a surface crystal at $n=44$ cannot be ruled out, the abrupt decrease in σ_1 is more likely due to the disappearance of the translational disorder along the chain axis which is one of the well-known characteristics of the bulk rotator phases, but is frozen out in the crystalline phase [43].

The increase of σ_1 with n, observed in Fig. 10(d) for $n<44$, is expected from capillary wave theory [35,54]. Since the surface tension at T_s is chain length independent (see Fig. 13) the variation in σ_1 with n is expected to result only from the corresponding n dependence of T_s, in the vicinity of which the σ_1 values for the various n were measured. However, the $\sigma_{cw}\sim\sqrt{T}$ thus predicted from Eq. (7) is too weak to account for the effect observed. Additional contributions, like the n dependence of σ_0 and/or $q_{\max}$, will have to be considered to account for the observed trend. Alternatively, models which exhibit a stronger T dependence, such as the $\sigma_{cw}\sim T$ predicted by Tkachenko and Rabin [55], will have to be invoked. The large scatter in the available σ_1 values precludes, however, a detailed disentanglement of the different contributions at this stage.

We conclude, therefore, that the ordered surface monolayer has three distinct structures: Two rotator phases, one for $n\leqslant30$ having surface-normal molecules and the other for $30<n<44$ with molecules tilted towards their nearest neighbors and one crystalline phase for $n\geqslant44$ with molecules tilted towards their next-nearest neighbors.

This trend very much follows the trend observed for the bulk. In the surface phase, the tilt sets in at a slightly higher n (C_{30} versus C_{26}) and the tilt direction is toward nearest neighbors while in the bulk, at the corresponding R_{IV} phase, it is towards next-nearest neighbors. The magnitudes of the tilt (θ), distortion(δ) and area per molecule (A) (both measured in a plane perpendicular to the chain axis), are comparable in the surface and bulk phases. The rotator to crystalline transition at the surface fits also well into this trend, since in the bulk the rotator phases were found [56] to disappear for $n>44$ where the bulk transition is directly from the liquid to the crystal.

D. Surface thermodynamics

The surface tension measurements of a complete cooling-heating cycle for C_{20} are shown in Fig. 5(b). The clear cusp marks T_s, the onset of surface freezing. At this temperature the slope of γ changes abruptly from a small negative value for $T>T_s$, typical of simple liquids, to a large positive value for $T<T_s$. This change is a clear indication of the formation of an ordered surface layer on top of the bulk liquid, as discussed above. The abruptness of the change indicates a first-order transition, with virtually no hysteresis and no pretransitional effects. The absence of any further slope changes implies that no additional structural transitions occur prior to bulk freezing [6], consistent with the x-ray results in Fig. 5(a).

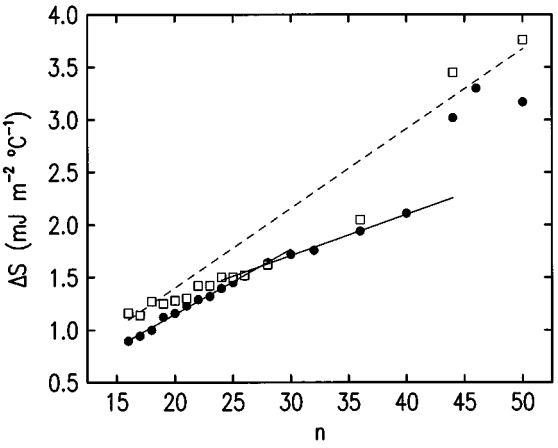

FIG. 11. The entropy change ΔS upon surface monolayer formation derived from the slopes of the surface tension measurements (closed circles). Note the break at $n\sim30$, where the tilted phase first occurs. The large increase at $n=44$ is associated with the rotator-to-crystalline surface phase transition. The open squares are the corresponding bulk values.

The slope for $T>T_s$ is relatively small and independent of n. For all alkanes measured, we obtain $(d\gamma/dT)_{T>T_s}=(-0.09\pm0.01)\text{mN m}^{-1}\,^\circ\text{K}^{-1}$, consistent with literature values [1,57]. Taking an average area per molecule of 20 Å^2, this yields a surface-bulk entropy difference of $(S_s-S_b)\approx 1.8\times10^{-23}$ J/°K$=k_b\ln 3.7$ per molecule, indicating about a fourfold increase in the number of available states for each surface molecule over one in the bulk. For $T<T_s$, the slope becomes positive, and its magnitude is larger and increases considerably with n, as shown by the solid circles in Fig. 11. The figure shows the slope difference above and below T_s, which equals the corresponding difference in the entropy: $\Delta(d\gamma/dT)=d\gamma/dT(T<T_s)-d\gamma/dT(T>T_s)\equiv\Delta S$.

One can compare the entropy change upon surface freezing with the entropy change upon bulk freezing from liquid to the rotator phases, properly normalized to a single monolayer. As shown by the open squares in Fig. 11, they are very close indeed. This good agreement leads, therefore, to two conclusions, both consistent with the x-ray measurements: (a) the surface phase is only one molecular layer thick and (b) the ordered monolayer for $n<44$ has a structure very similar to that of the bulk rotator phase. The systematic deviation of ΔS from the bulk rotator liquid values at low n, as seen in Fig. 11, can be explained by the fact that for $n<22$, the surface rotator phase is hexagonal, while the bulk melts directly from the distorted and more ordered R_I phase. The bulk R_{II} to R_I transition is first order and the entropy of that transition extrapolated to shorter chain lengths could account for that deviation [15]. It has been shown that the interlayer coupling is important in establishing the distortion of the R_I phase [2,16] and thus, it is not surprising that the surface phase is R_{II} even where the bulk melts directly from the R_I phase.

As shown in Fig. 11, ΔS has an approximately linear dependence on n for $n<44$. This can be rationalized by considering the most dominant contribution to the entropy: the chain conformation degrees of freedom. Successive C—C bonds in a chain can have two *gauche* and one *trans* conformations, with the latter having the lowest energy [58(a)]. Approximating the chains in the liquid state to be completely flexible and free from any steric hindrance so that each bond conformation is of equal probability the entropy per chain is $S_{T>T_s,calc}=k_B\ln(3^{n-3})$ where k_B is the Boltzmann constant. Upon ordering, the conformational degrees of freedom of chains on the surface are greatly reduced, and all bonds are assumed to be *trans*, and have approximately zero entropy, $S'_{T<T_s,calc}\approx 0$. Thus, we obtain $\Delta S_{calc}=\Delta(d\gamma/dT)_{calc}=k_B[(n-3)\ln 3]=1.52\times10^{-23}\times n-4.55\times10^{-23}$ J/K. This approximation, shown as a dashed line in Fig. 11, provides an upper limit on the possible conformational entropy loss upon surface freezing. As expected, it systematically overestimates the experimental values, but accounts reasonably well for the linear n dependence of the slope. The overestimation comes mainly from the gross approximation of zero entropy for the surface crystalline phase and an equal probability for the *trans* and *gauche* bonds in the liquid phase. Finally, the entropy for the crystalline phase is generally nonzero, and varies with the crystalline structures. The calculation and understanding of the melting entropy of the bulk alkanes has progressed well beyond the simple approximation given above [58(b)].

Examining more closely the n dependence of ΔS, plotted as a solid line in Fig. 11, one can observe a change of slope at $n\approx 30$, to a lower slope for $n>30$ than that for $n<30$. The change of slope marks the nontilt-tilt transition of the molecules in the crystalline layer, discussed above. Part of this slope change is attributable to the change in the area per molecule. Furthermore, ΔS for $n\geqslant 44$ takes values much larger than those for $n<44$, indicating another structural transition in the surface crystalline layer. A similarly large jump of ΔS has been observed for the C_{36} crystalline surface monolayer in $\text{C}_{26}/\text{C}_{36}$ mixtures, where it was shown to be due to a transition where the direction of the tilt changes from nearest neighbors to next-nearest neighbors. X-ray measurements confirm that the C_{44} molecules in the surface crystals indeed tilt towards next-nearest neighbors, as shown by the Bragg rod in Fig. 8(f).

The large jump in ΔS at $n\approx 44$ results from a sharp decrease in the surface entropy. Since the only degrees of freedom remaining in the frozen surface layers are the rotational ones, it is likely that the jump marks the freezing out of the rotations and the formation of a true crystalline surface phase for $n\geqslant 44$. This supports the conclusion of a rotator-to-crystalline phase transition in the surface layer, drawn from the x-ray measurements discussed above. The open squares in Fig. 11, for $n\geqslant 44$ only, are the bulk entropies [59] for the crystal-liquid transition without the intervening rotator phase. These are closer to the surface phase data points than those of the rotator phases. However, the fact that they are higher suggests that the surface crystal phases have a larger entropy (disorder) than the corresponding bulk phases, which is reasonable in view of the reduced molecular confinement at the surface.

Finally, note that the transition (with n) between the two tilted phases near $n\approx 44$ should be viewed as mostly a rotator-crystal transition, with the tilt direction change being a rather minor subtlety. This is distinct from the L_{β_I} to L_{β_L} to L_{β_F} transitions [38] in phospholipids, for example, where the *only* parameter changing is the tilt direction. This is clearly demonstrated by the large magnitude of the entropy change observed for C_{44}. For a first-order tilt direction transition this change is negligible [51], while for a bulk rotator-crystal transition it is very large [1].

E. Temperature range of existence

The temperature ranges of existence $\Delta T=T_s-T_f$ of the crystalline surface phase, as obtained from both surface tension and x-ray reflection measurements (for an example see Fig. 5), agree excellently with each other for all chain lengths. ΔT has a nonmonotonic n dependence, plotted in Fig. 12, showing the surface crystalline phase to appear only for $16\leqslant n\leqslant 50$ and to have a maximum range of $\Delta T\approx 3\,^\circ\text{C}$ for $n\approx 20$.

This phase diagram, ΔT vs n, can be accounted for by free energy considerations, as follows. Noting that the free energy of the bulk liquid is equal to that of the bulk solid at T_f, and the free energy of surface liquid equals that of the surface solid at T_s, one may calculate the temperature range ΔT as

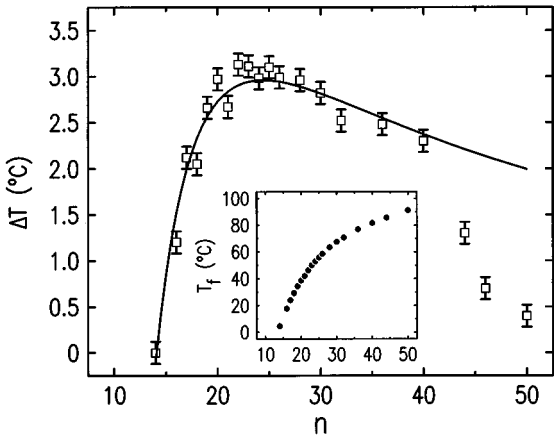

FIG. 12. The temperature range of existence ΔT for the surface crystalline phase. The solid line is the theoretical expression derived in the text, and the inset charts the bulk freezing temperatures vs n.

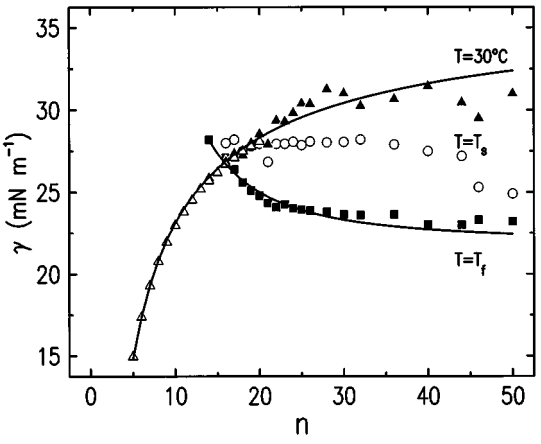

FIG. 13. The surface tension dependence on n at a fixed $T=30°$, surface transition T_s, and bulk freezing T_f. The solid lines are the theoretical expressions discussed in the text.

$$\Delta T = \frac{\gamma_{T_s} - \gamma_{T_f}}{S - S'}, \tag{14}$$

where γ_{T_f} and γ_{T_s} are the surface tensions at the bulk freezing and surface freezing points, and S and S' are the entropies for the surface liquid and surface crystalline phases, respectively. At a given temperature, say $T=30\,°\mathrm{C}$, chain-end free volume considerations [58(a)] yield for the surface tension an n-dependence form: $A-B/n^{2/3}$, (where A and B are constants) which is shown in Fig. 13 to fit the experiment well with $A=37.2$ mN/m and $B=65.4$ mN/m. For alkanes whose T_s is above the given $T=30\,°\mathrm{C}$, the value extrapolated from the liquid surface phase is used in the figure. The surface tension values at the onset of the surface crystalline phase γ_{T_s} (the open circles in Fig. 13) are found to be approximately constant over the measured n range, $\gamma_{T_s} \approx c = 28$ mN/m. Note that since $d\gamma/dT$ is rather small in this temperature range, $\gamma(T_s)$ is practically the same as the values of the surface tension extrapolated to the bulk freezing point from the high temperature phase, which is n independent. Although we do not know the physical origin of this n independence, we do notice that many physical quantities besides the surface tension, such as the density and the viscosity are practically independent of the chain length at their respective bulk freezing points.

The n dependence of γ_{T_f} can be understood by noting that the excess free energy of a monolayer at the surface over one inside the bulk solid is due to the missing interactions with the nonexistent overlayers above the surface. Assuming that the dominant interaction is van der Waals (vdW) type, the excess free energy varies as $1/d^2$, where $d \sim n$ is the layer thickness [60]. It is easy to show that for this case the expected n dependence of γ_{T_f} is $\gamma_{T_f} = \gamma'_\infty + \beta/n^2$. This dependence is indeed found in our measurements, with $\gamma'_\infty = 22.0$ mN/m and $\beta = 1200$ mN/m. With this dependence, the shorter the chain, the larger the vdW free energy penalty that has to be paid for the formation of the monolayer at the surface over that in the bulk. This increasing penalty is expected, therefore, to impose a short length limit on the surface freezing effect, as indeed found at $n \approx 14$, where the system presumably reverts to either the common surface melting behavior or to the melting of the bulk and surface at the same temperature. Unfortunately, technical difficulties in preparing well-defined surfaces preclude x-ray measurements in this region.

Besides the energies, the competing entropy effect has to be considered. As discussed above, for $n<44$ the entropy loss upon transition from the liquid to the rotator phase increases linearly with length: $S-S' \sim n$. Considering the n dependence of both the energy and entropy, ΔT can be calculated from Eq. (14) as

$$\Delta T \approx \frac{1}{n}\left(c - \gamma'_\infty - \frac{\beta}{n^2}\right) = \frac{a}{n} - \frac{b}{n^3}, \tag{15}$$

where a and b are positive constants. Equation (15) clearly shows that for a small enough $n, \Delta T$ is negative: the surface layer disorders below the bulk freezing temperature T_f, i.e., the common surface melting occurs. As n increases past $n \approx 14$, ΔT becomes positive and surface freezing occurs with a nonzero temperature range. However, for very large n, the entropy shrinks the ordered surface phase to a small temperature range: $\Delta T \to 0$ for $n \to \infty$. Only for intermediate n does an ordered surface phase exist with a significant temperature range. Fitting the measured data for $n<44$ by Eq. (15) yields a satisfactory agreement, as shown by the solid line in Fig. 12. The fast falloff in Fig. 12 for $n \geqslant 44$ is clearly induced by the considerably greater surface entropy loss accompanying the rotator-to-crystal surface phase transition discussed above and shown in Fig. 11. The longer chains and the correspondingly higher temperatures also result in a proliferation of *gauche* conformations in the chains. The increased deviation from a uniform shape and a constant cross section along the chain will further reduce the tendency to form an ordered crystalline layer. This also contributes to the fast decrease in ΔT.

F. Interface energies and surface freezing

The experimental results discussed above can be used to obtain values for the solid-liquid and solid-vapor interfacial

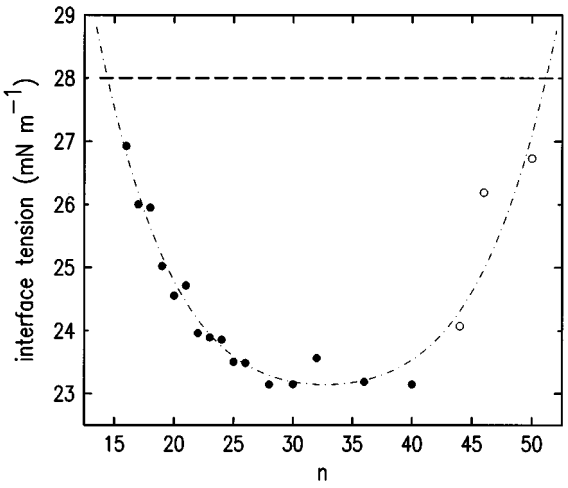

FIG. 14. The total excess surface energies γ_l (dashed line) and $\gamma_s+\gamma_{sl}$ (solid circles for $n<44$ and open circles for $n\geqslant 44$), both at $T=T_f$. The dot-dash line is a smooth guide to the eye only, representing $\gamma_s+\gamma_{sl}$. The constant $\gamma_l(T_f)\approx 28$ mN/m is determined from Ref. [1] and the present measurements. Surface freezing occurs when $\gamma_s+\gamma_{sl}<\gamma_l$. Using the intersections of the dot-dash and the dashed lines, this condition is fulfilled here for $14<n\leqslant 50$, as indeed observed experimentally. Further details are given in the text.

energies, which are inaccessible to direct measurements. A careful examination of the relative magnitudes of these values yields important insight into the conditions for the occurrence of surface freezing. The formation of the surface crystalline layer entails the formation of a solid-liquid and a solid-vapor interface, with energy costs of γ_{sl} and γ_s, respectively. The elimination of the liquid-vapor surface results in an energy gain of $\gamma_l(T)=\gamma_0-TS_l$, where $\gamma_0=\gamma_l(T=0)$ is the energy contribution, and S_l is the excess surface entropy [61]. The energy balance dictates that the surface crystallizes if by doing so the energy is reduced, i.e., if $\gamma_s+\gamma_{sl}<\gamma_l$. Defining $\delta\gamma=\gamma_l(T_f)-\gamma_s$, the surface freezing condition can also be written as $\delta\gamma>\gamma_{sl}$. The range of existence of the surface phase is

$$\Delta T=(\delta\gamma-\gamma_{sl})/(\Delta S+S_l)=[\gamma_l(T_f)-(\gamma_s+\gamma_{sl})]/(\Delta S+S_l), \tag{16}$$

where the temperature dependences of γ_s and γ_{sl} were neglected. Likewise, surface *melting* would occur when $-\delta\gamma>\gamma_{sl}$, and no surface-specific transition would occur where $-\gamma_{sl}<\delta\gamma<\gamma_{sl}$.

Taking the measured surface tension values of $\gamma_l(T_f)$ from our work as well as the literature [62], we chose a constant $\gamma_l(T_f)\approx 28$ mN/m over the n range of interest. While various n dependences have been predicted for this quantity, the uncertainty in the experimental data is greater than any n dependence in the n range under discussion. Using this $\gamma_l(T_f)$ value in Eq. (16) and values of $\Delta S\Delta T$ as measured in this work we calculated the sum of surface energies $\gamma_s+\gamma_{sl}$. These are plotted in Fig. 14. Using the intersections of the $\gamma_s+\gamma_{sl}$ vs n curve (represented by the dot-dash guide-to-the-eye line) with γ_l (represented by the roughly constant dashed line), we see that the surface freezing condition $\gamma_s+\gamma_{sl}<\gamma_l$ is, indeed, fulfilled down to $n\approx 14$ only, where the surface freezing effect is observed experimentally to vanish. On the high-n side the rotator-crystal surface phase transition at $n=44$ results in an abrupt increase of ~ 3 mN/m in the measured $\gamma_s+\gamma_{sl}$ (open circles), causing it to intersect γ_l at $n\approx 52$. This, again, invalidates the surface freezing condition, and causes the effect to vanish for $n>50$.

To separate $\gamma_s+\gamma_{sl}$ into its components, additional independent data is required. Such data for the various alkane phases is, however, very scarce. Some of the best data available is due to Zisman and co-workers [63] whose contact angle measurements of liquid C_{16} against a single crystal *00l* face of C_{36} gave $\gamma_s-\gamma_{sl}=19.2$ mN/m. Assuming this value to apply also for the physically unattainable C_{16}(liquid)—C_{16}(crystal) interface, and combining them with our data for $\gamma_s+\gamma_{sl}=26.93$ mN/m, from Fig. 14, we obtain: $\gamma_s=23.07$ mN/m and $\gamma_{sl}=3.87$ mN/m for C_{16}. Assuming Zisman's value to apply to the C_{36}(liquid)—C_{36}(crystal) interface, where $\gamma_s+\gamma_{sl}=23.19$ mN/m, yields $\gamma_s=21.20$ mN/m and $\gamma_{sl}=2.00$ mN/m for C_{36}. In either case it is clear that the contribution to the surface energy from the solid-liquid interface is much less than that from the liquid-vapor interface.

We wish to point out that measuring the contact angle against an *00l* surface of a single crystal rather then against a much more readily available polycrystalline solid is of crucial importance. In the former case the liquid is in contact with a layer of terminal CH_3 groups, mimicking accurately the geometry of the surface-crystal/bulk-liquid interface in our measurements. By contrast, the surface of a polycrystalline sample is a random mixture of CH_3 and CH_2 groups, and thus will yield a different contact angle against the liquid, resulting in different surface energies. This is very well demonstrated by homogeneous nucleation experiments in n-alkane melts, which yield an average surface energy (σ) for the solid-liquid interface, without distinguishing between the ''sides''(CH2) γ'_{sl} and ''ends''(CH3) γ_{sl} of the crystallites [64,65], where [66] $\gamma'^2_{sl}\cdot\gamma_{sl}=(2/3)\sigma^3$. Since we have deduced γ_{sl}, we can use σ to calculate γ'_{sl}. Using values for σ from Turnbull and Spaepen [64] of 10.4 and 11 mN/m for C_{16} and C_{36}, respectively, we compute $\gamma'_{sl}=13.9$ mN/m for C_{16} and $\gamma'_{sl}=21.1$ mN/m for C_{36}, which yields a ratio of $\gamma_{sl}/\gamma'_{sl}=0.28$ and 0.095 for these alkanes, respectively. That this ratio is much less than unity implies that the surface energy density of the CH_3 terminated surface is much less than that of the CH_2 terminated one, and supports the finding that the molecules do not lie flat at the interface. This finding is vastly different from the $\gamma_{sl}/\gamma'_{sl}\approx 17$ obtained by Cormia, Price, and Turnbull [65] for the polyethylene(solid)–C_{18}(liquid) interface where the polyethylene surface is not dominated by terminal methyls, but rather by the high-energy bends in the polymeric CH_2 chain, resulting in $\gamma_{sl}\gg\gamma'_{sl}$.

A more detailed study of the chain length and temperature dependence of the individual interfacial energies of the various surfaces in the different phases is certainly desirable. However, we have been able to determine γ_s,γ_{sl}, and γ'_{sl} individually, and demonstrate that our results, in conjunction with the appropriate contact angle data, allow an accurate determination of these directly inaccessible surface energies.

IV. CONCLUSION

We presented here a study of surface freezing in normal-alkane melts, which results in the formation of a crystalline monolayer on the surface of the bulk liquid, at a temperature T_s, a few degrees above its freezing temperature T_f. This is a rare phenomenon, since other materials (except liquid crystals) exhibit surface melting. The study employed temperature (T) and molecular length (n)-dependent x-ray reflectivity, grazing incidence diffraction, and surface tension measurements. The results of these measurements are summarized in Table I. The following results and conclusions emerge from the study:

(1) For $T>T_s$ the width of the liquid surface density profile is capillary wave dominated, with a width of $\sim$4.4 Å, expected from capillary wave theory for the surface tension measured.

(2) The ordered surface layer formed at T_s is an hexagonally packed monolayer with vertically aligned molecules for $n<30$, tilted towards nearest neighbors for $30\leqslant n<44$ and tilted towards next-nearest neighbors for $n\geqslant 44$.

(3) The surface monolayer is in a rotator phase for $n<44$ and in a nonrotator, crystalline phase for $n\geqslant 44$.

(4) The tilt angle is n dependent, and rises continuously from $<5°$ for C_{30} to $\sim 23°$ for C_{44}.

(5) The packing in the surface plane remains nearly hexagonal for the measured molecular lengths, even though perpendicular to the molecular axis the packing is distorted from the hexagonal (i.e., $\delta>0$).

(6) The molecular tilt is accompanied by an increase in the in-plane lattice constants.

(7) The single monolayer formed at T_s persists down to T_f for all alkanes. No further layers are formed. As a wetting phenomenon, the monolayer formation is classified as a partial wetting.

(8) The ordered monolayer phase appears only for molecular lengths of $16\leqslant n\leqslant 50$, within a temperature range of up to $\sim 3\,°C$ above T_f.

(9) The disappearance of the surface phase for $n\leqslant 14$ can be interpreted as a surface freezing to surface melting transition.

(10) The decrease in ΔT for $n\geqslant 44$ and the eventual disappearance of the effect at $n>50$ are probably due to an increased packing frustration in the more ordered crystalline, rather than rotator, surface phase for $n\geqslant 44$. A contribution to the frustration from the proliferation of intrachain *gauch* transformations at these longer, higher melting-temperature chains is very likely.

(11) A simple model based on the free energy of the available conformational degrees of freedom, which corresponds to the entropy of the bulk melting transition, accounts quantitatively for the n dependence of the surface tension slope change at T_s.

(12) A related model, based on the variation of entropy and excess van der Waals free energy with chain length in the surface layer accounts very well for the n dependence of the temperature range of existence of the surface crystalline layer $\Delta T=T_s-T_f$.

(13) The tilting transition and the n dependence of the tilt probably result from the competing effects of a decreased chain distance and decreased chain overlap on the interchain attraction upon tilting.

(14) The condition for surface freezing is $\gamma_s+\gamma_{sl}<\gamma_l(T_f)$. For the alkanes exhibiting surface freezing our data indicates that this condition is indeed fulfilled.

(15) $\gamma_s+\gamma_{sl}$ is larger for the crystal phase than for the rotator phase by a few mN/m. This invalidates the surface freezing condition for $n\approx 50$ and above, and causes the vanishing of the effect.

(16) In conjunction with the appropriate contact angle data, our results yield values for the *individual* surface energies γ_s and γ_{sl}, which are otherwise inaccessible to experiment. γ_{sl} is found to be much smaller than γ_s, γ_l, or γ'_{sl}.

(17) For a surface consisting of methyl end groups, as is the case in our measurements, γ_{sl} is much smaller than for surfaces consisting of predominantly CH_2 groups, such as polymers and polycrystalline alkanes.

Several important issues are, however, still outstanding. The most important of these is a quantitative microscopic theoretical description of the monolayer formation and its behavior with T and n. In particular, it will have to explain why surface freezing is favored over melting in this particular case. We have observed the appearance of surface freezing in a number of other chain molecules like alcohols [67] and diols as well as mixtures of these molecules [9]. These results strongly indicate that the chain-like structure plays an important role in the occurrence of surface freezing rather than melting. One attempt to account for this assumes that the lower density of the CH_3 end groups imparts them a slightly higher surface activity. The surface enrichment of the end groups will induce some vertical preferential alignment of the alkane chains even at temperatures higher than T_s, and lead eventually to a more ordered phase at the surface. This picture is supported by simulations [68], lattice gas calculations [69], and nonlinear optics measurements on alkane melts [70]. Tkachenko and Rabin [55] suggested recently that the crystalline surface layer may be stabilized by fluctuations along the molecular axis, which are suppressed in the bulk. The length of the chain molecules and their alignment allow large fluctuations, and hence a sufficiently large entropic contribution, without violating the Lindemann criterion for crystal melting. In smaller molecules this may not be possible. This explains both the role of the chain structure in the occurrence of the surface freezing effect and the lower limit on the chain length at which this phenomenon occurs. While this theory accounts successfully for the (n,T) phase diagram and several other features of the experimental results, its generality will have to be tested on other-molecules as well.

We hope that the study presented here, as well as in our forthcoming publications dealing with other chain molecules exhibiting similar effects like alcohols, alkane mixtures, etc., will stimulate additional theoretical work and lead to a better understanding of the rare surface freezing effect presented here.

ACKNOWLEDGMENTS

We gratefully acknowledge support by the U.S.-Israel Binational Science Foundation, Jerusalem, and the State of Illinois under HECA. B.N.L. is supported by the Division of Materials Research, DOE under Contract No. DE-AC02-76CH00016.

[1] D. M. Small, *The Physical Chemistry of Lipids* (Plenum, New York, 1986).
[2] E. B. Sirota, H. E. King Jr., H. H. Shao, and D. M. Singer, J. Phys. Chem. **99**, 798 (1995).
[3] A. Müller, Proc. R. Soc. London, Ser. A **138**, 514 (1932).
[4] A. Craievich, J. Doucet, and I. Denicolo, Phys. Rev. B **32**, 4164 (1985), and references therein.
[5] G. Ungar, J. Phys. Chem. **87**, 689 (1983); G. Ungar and N. Masic, J. Phys. Chem. **89**, 1036 (1985).
[6] X. Z. Wu, E. B. Sirota, S. K. Sinha, B. M. Ocko, and M. Deutsch, Phys. Rev. Lett. **70**, 958 (1993).
[7] X. Z. Wu, B. M. Ocko, E. B. Sirota, S. K. Sinha, M. Deutsch, B. H. Cao, and M. W. Kim, Science **261**, 1018 (1993).
[8] X. Z. Wu, B. M. Ocko, E. B. Sirota, S. K. Sinha, and M. Deutsch, Physica A **200**, 751 (1993).
[9] X. Z. Wu, B. M. Ocko, H. Tang, E. B. Sirota, S. K. Sinha, and M. Deutsch, Phys. Rev. Lett. **75**, 1332 (1995).
[10] J. C. Earnshaw and C. J. Hughes, Phys. Rev. A **46**, R4494 (1992).
[11] T. Pfhol, D. Beaglehole, and H. Riegler, Chem. Phys. Lett. **260**, 82 (1996).
[12] B. M. Ocko, A. Braslau, P. S. Pershan, J. Als-Nielsen, and M. Deutsch, Phys. Rev. Lett. **57**, 94 (1986).
[13] B. Ocko, Phys. Rev. Lett. **64**, 2160 (1990).
[14] J. Als-Nielsen, F. Christensen, and P. S. Pershan, Phys. Rev. Lett. **48**, 1107 (1982); P. S. Pershan and J. Als-Nielsen, Phys. Rev. Lett. **52**, 759 (1984).
[15] E. B. Sirota and D. M. Singer, J. Chem. Phys. **101**, 10 873 (1994).
[16] E. B. Sirota, D. M. Singer, and H. E. King, Jr., J. Chem. Phys. **100**, 1542 (1994).
[17] E. B. Sirota, H. E. King, Jr., D. M. Singer, and H. H. Shao, J. Chem. Phys. **98**, 5809 (1993).
[18] J. G. Dash, Contemp. Phys. **30**, 89 (1989); R. Lipowsky, J. Appl. Phys. **55**, 2485 (1984); G. An and M. Schick, Phys. Rev. B **37**, 7534 (1988).
[19] J. W. M. Frenken and J. F. van der Veen, Phys. Rev. Lett. **54**, 134 (1985); H. Dosch, T. Höfer, J. Peisl, and R. L. Johnson, Europhys. Lett. **15**, 527 (1991); D. M. Zhu and J. G. Dash, Phys. Rev. Lett. **57**, 2959 (1986); M. Elbaum and M. Schick, Phys. Rev. Lett. **66**, 1713 (1991); S. Chandavarkar, R. M. Geertman, and W. H. de Jeu, Phys. Rev. Lett. **69**, 2384 (1992).
[20] G. J. Kellogg, P. S. Pershan, E. H. Kawamoto, W. Foster, M. Deutsch, and B. M. Ocko, Phys. Rev. E **51**, 4709 (1995).
[21] E. B. Sirota, P. S. Pershan, S. Amador, and L. B. Sorensen, Phys. Rev. A **35**, 2283 (1987).
[22] B. S. Swanson, H. Stragier, D. J. Tweet, and L. B. Sorensen, Phys. Rev. Lett. **62**, 909 (1989).
[23] D. E. Moncton, R. Pindak, S. C. Davey, and G. S. Brown, Phys. Rev. Lett. **49**, 1865 (1982).
[24] R. H. Tregold, *Order in Thin Organic Films* (Cambridge University Press, Cambridge, England, 1994); A. Ulman, *An Introduction to Ultrathin Organic Films: From Langmuir Blodgett to Self Assembly* (Academic, Boston, 1991).
[25] G. M. Bomarito, W. J. Foster, P. S. Pershan, and M. L. Schlossman, J. Chem. Phys. **105**, 5265 (1996).
[26] G. L. Gaines, *Insoluble Monolayers at the Liquid Gas Interface* (Wiley, New York, 1966).
[27] D. Jacqumain, S. Grayer Wolf, F. Leveiller, M. Deutsch, K. Kjaer, J. Als-Nielsen, M. Lahav, and L. Leiserowitz, Angew. Chem. Int. Ed. Engl. **31**, 130 (1992); J. Als-Nielsen, D. Jacquemain, K. Kjaer, F. Leveiller, M. Lahav, and L. Leiserowitz, Phys. Rep. **246**, 251 (1994).
[28] V. M. Kaganer and E. B. Loginov, Phys. Rev. E **51**, 2237 (1995); V. M. Kaganer, I. R. Peterson, R. M. Kenn, M. C. Shih, M. Durbin, and P. Dutta, J. Chem. Phys. **102**, 9412 (1995).
[29] X. Z. Wu, B. Ocko, E. B. Sirota, and M. Deutsch (unpublished).
[30] H. Yinnon and D. R. Uhlmann, J. Non Cryst. Solids **44**, 37 (1981).
[31] R. K. Thomas (private communication).
[32] M. Born and E. Wolf, *Principles of Optics* (Pergamon, Oxford, 1975).
[33] F. Abeles, Ann. Phys. (Paris) **5**, 596 (1950).
[34] A. Braslau, P. S. Pershan, G. Swislow, B. M. Ocko, and J. Als-Nielsen, Phys. Rev. A **38**, 2457 (1988); M. K. Sanyal, S. K. Sinha, K. G. Huang, and B. M. Ocko, Phys. Rev. Lett. **66**, 628 (1991).
[35] B. M. Ocko, X. Z. Wu, E. B. Sirota, S. K. Sinha, and M. Deutsch, Phys. Rev. Lett. **72**, 242 (1994).
[36] J. Als-Nielsen and K. Kjaer, in *Phase Transitions in Soft Condensed Matter*, edited by T. Riste and D. Sherrington (Plenum, New York, 1989), p. 245.
[37] D. K. Schwartz, M. L. Schlossman, and P. S. Pershan, J. Chem. Phys. **96**, 2356 (1991).
[38] G. S. Smith, E. B. Sirota, C. R. Safinya, R. J. Plano, and N. A. Clark, J. Chem. Phys. **92**, 4519 (1990).
[39] G. Vineyard, Phys. Rev. B **26**, 4146 (1982).
[40] C. A. Croxton, *Statistical Mechanics of the Liquid Surface* (Wiley, New York, 1980).
[41] B. Berge, L. Fancheux, K. Schwab, and A. Libchaber, Nature **350**, 322 (1991).
[42] A. Braslau, M. Deutsch, P. S. Pershan, A. Weiss, J. Als-Nielsen, and J. Bohr, Phys. Rev. Lett. **54**, 114 (1985); S. K. Sinha, E. B. Sirota, S. Garoff, and H. B. Stanley, Phys. Rev. B **38**, 2297 (1988); A. Braslau, P. S. Pershan, and G. Swislow, Phys. Rev. A **38**, 2457 (1989).
[43] A. Craievich, I. Denicolo, and J. Doucet, Phys. Rev. B **30**, 4782 (1984).
[44] B. Ewen, G. R. Strobl, and D. Richter, Faraday Discuss. Chem. Soc. **69**, 19 (1980).
[45] The broad GID liquid *surface* peak shown in Fig. 2 of Ref. [6] was subsequently verified to be a *bulk* liquid peak. The surface crystalline GID peak shown in the same figure is, however, correct.
[46] A. Habenshuss and A. H. Narten, J. Chem. Phys. **92**, 5692 (1990); G. W. Stewart, Phys. Rev. **31**, 174 (1928).
[47] The data are not good enough to distinguish between quasi- and true-long-range order.
[48] M. Maroncelli, H. L. Strauss, and R. G. Snyder, J. Chem. Phys. **82**, 2811 (1985).
[49] W. L. Jarrett, L. J. Mathias, R. G. Alamo, L. Mandelkern, and D. L. Dorset, Macromolecules **25**, 3468 (1992).
[50] L. Askadskaya and J. P. Rabe, Phys. Rev. Lett. **69**, 1395 (1992); J. P. Rabe and S. Buchholz, Science **253**, 424 (1991).
[51] J. Budai, R. Pindak, S. C. Davey, and J. Goodby, J. Phys. Lett. (Paris) **45**, L-1053 (1984).
[52] R. D. Heyding, K. E. Russell, T. L. Varty, and D. St-Cyr, Powder Diffr. **5**, 93 (1990).
[53] J. Daillant, L. Bosio, J. J. Benattar, and J. Meunier, Europhys. Lett. **8**, 5 (1989); J. Meunier, J. Phys. (Paris) **48**, 1819 (1987).

[54] J. R. Rowlinson and B. Widom, *Molecular Theory of Capillarity* (Clarendon, Oxford, 1982); M. P. Gelfand and M. E. Fisher, Physica A **166**, 1 (1990).
[55] A. V. Tkachenko and Y. Rabin, Phys. Rev. Lett. **76**, 2527 (1996); Phys. Rev. E **55**, 778 (1997).
[56] G. Ungar, Macromolecules **19**, 1317 (1986).
[57] J. Timmermans, *Physico-Chemical Constants of Pure Organic Compounds* (American Elsevier, New York, 1965); C. I. Poser and I. C. Sanchez, J. Coll. Interf. Sci. **69**, 539 (1979).
[58] (a) P.-G. de Gennes, *Scaling Concepts in Polymer Physics* (Cornell, Ithaca, 1979). (b) See for example: A. Würflinger, Coll. Poly. Sci. **262**, 115 (1984).
[59] M. G. Broadhurst, J. Res. Nat. Bur. Stand. **66A**, 241 (1962); Y. Jin and B. Wunderlich, J. Phys. Chem. **95**, 9000 (1991).
[60] J. N. Israelachvili, *Intermolecular and Surface Forces* (Academic, Orlando, 1985); J. Mahanty and B. W. Ninham, *Dispersion Forces* (Academic, New York, 1976).
[61] X. Z. Wu, H. H. Shao, B. M. Ocko, M. Deutsch, S. K. Sinha, M. W. Kim, H. E. King, Jr., and E. B. Sirota, in *Dynamics in Small Confining Systems*, edited by J. M. Drake, S. M. Troian, J. Klafter, and R. Kopelman (MRS, Pittsburgh, 1995), Vol. 366.
[62] J. J. Jasper, J. Phys. Chem. Ref. Data **1**, 914 (1972); F. D. Rossini, K. S. Pitzer, R. L. Arnett, R. M. Braun, and G. C. Pimentel, *Selected Values of Physical and Thermodynamic Properties of Hydrocarbons and Related Compounds* (Carnegie Press, Pittsburgh, 1953); G. T. Dee and B. B. Sauer, J. Colloid and Interf. Sci. **152**, 85 (1992).
[63] H. W. Fox and W. A. Zisman, J. Coll. Sci. **7**, 428 (1952); W. A. Zisman, in *Contact Angle, Wettability and Adhesion*, edited by F. M. Fowkes (American Chemical Society, Washington, DC, 1964).
[64] D. Turnbull and F. Spaepen, J. Poly. Sci. **63**, 237 (1978).
[65] R. L. Cormia, F. P. Price, and D. Turnbull, J. Chem. Phys. **37**, 1333 (1962).
[66] M. J. Oliver and P. D. Calvert, J. Cryst. Growth **30**, 343 (1975).
[67] M. Deutsch, X. Z. Wu, E. B. Sirota, S. K. Sinha, B. M. Ocko, and O. M. Magnussen, Europhys. Lett. **30**, 283 (1995).
[68] T. K. Xia, J. Ouyang, M. W. Ribarsky, and U. Landman, Phys. Rev. Lett. **69**, 1967 (1992); J. G. Harris, J. Phys. Chem. **96**, 5077 (1992).
[69] F. A. M. Leermakers and M. A. Cohen Stuart, Phys. Rev. Lett. **76**, 82 (1996).
[70] G. A. Sefler, G. Du, P. B. Miranda, and Y. R. Shen, Chem. Phys. Lett. **235**, 347 (1995).